Marine Geology 437 (2021) 106488

Contents lists available at ScienceDirect

Marine Geology

journal homepage: www.elsevier.com/locate/margo

Invited Research Article

Paleoceanographic and paleoclimatic variability in the Western Mediterranean during the last 25 cal. kyr BP. New insights from contourite drifts

B. Alonso [a,*], C. Juan [b], G. Ercilla [a], I. Cacho [c], N. López-González [d], F.J. Rodríquez-Tovar [e], J. Dorador [f], G. Francés [g], D. Casas [a], T. Vandorpe [h], J.T. Vázquez [d]

[a] Instituto de Ciencias del Mar-CSIC, P. Marítim 37, 08003 Barcelona, Spain
[b] University of Lille, CNRS, Univ. Littoral Côte d'Opale, UMR 8187 - LOG - Laboratoire d'Océanologie et de Géosciences, F-59000 Lille, France
[c] Universidad de Barcelona, Facultad de Ciencias de la Tierra, Martí i Franquès, s/n, 08028 Barcelona, Spain
[d] Instituto Español de Oceanografía, C.O. de Málaga, Puerto Pesquero s/n, 29649 Fuengirola, Spain
[e] Universidad de Granada, Departamento de Estratigrafia y Paleontología, Avenida Fuentenueva s/n, 18002 Granada, Spain
[f] Department of Earth Sciences, Royal Holloway University of London, Egham Hill, Egham TW20 0EX, UK
[g] Universidad de Vigo, Facultad de Ciencias del Mar, Campus Universitario Lagoas, 36200 Vigo, Spain
[h] Flanders Marine Institute (VLIZ), Wandelaarkaai 7, 8400 Oostende, Belgium

ARTICLE INFO

Editor: Michele Rebesco

Keywords:
Contourites
Sortable silt
Western Mediterranean Deep Water
Paleoceanography
Alboran Sea

ABSTRACT

The Western Mediterranean Deep Water (WMDW), on its way out toward the Atlantic Ocean, has favored the formation of contourite drifts in the Alboran Sea (SW Mediterranean) since the opening of the Strait of Gibraltar. Resolving the nature of these deposits is crucial for reconstructing the WMDW variability at a millennial scale, deciphering its bottom current paleo-velocity, and establishing paleoclimatic implications over the last 25 cal. kyr BP. Two sediment cores retrieved from elongated separated and plastered contourite drifts formed along its path are investigated by means of multi-sedimentological data (terrigenous grain-size, sortable silt, terrigenous and carbonate sediment fluxes, bioturbation and ichnofabric changes), geochemical data (Zr/Al and Si/(Si + Al) ratios), chronostratigraphic data ($\delta^{18}O$, and ^{14}C data) as well as statistical analyses (grain-size end-member modelling and spectral analysis). Integration of these data confirms the contouritic nature of Alboran drift deposits. The high-resolution paleocurrent records of the WMDW inferred from the sortable silt of contourite sequences led us to define two regimes in terms of WMDW flow energy. Regime 1 (weak to moderate velocity) defined by paleo-velocities of ~4 to 23 cm s^{-1} is dominant during the last 24 cal kyr BP. Regime 2 (strong velocity) is characterized by estimated paleo-velocities of about ~36 cm s^{-1} during Heinrich Stadial 2. The spectral analysis of bottom current proxies (sortable silt and Zr/Al ratio) matches four cyclic climatic signals (1900 yr, 2300 yr, 4000 ye and 6100 yr), corroborating the occurrence of millennial-scale cyclicity. These cycles are related to atmospheric climate variability, in turn linked to variations in solar activity. Our results, when combined with published data from a neighboring NW Mediterranean contourite drift, provide for a better regional understanding of the WMDW millennial-scale dynamics.

1. Introduction

Contourite drifts are defined as mounded or sheeted sedimentary bodies shaped largely by alongslope thermohaline and wind-driven bottom currents (Stow and Lowell, 1979; Stow et al., 2002; Rebesco and Carmelenghi, 2008). Contourite drifts are ubiquitous on ocean floors: they occur from the abyssal plains (Cremer et al., 1993; Bianchi et al., 2001) to upper shelf regions (Verdicchio and Trincardi, 2008). Yet they are particularly frequent along continental slopes, where the Coriolis effect and irregular seafloor morphology condition bottom current

* Corresponding author.
E-mail addresses: belen@icm.csic.es (B. Alonso), gemma@icm.csic.es (G. Ercilla), icacho@ub.edu (I. Cacho), nieves.lopez@ieo.es (N. López-González), fjrtovar@ugr.es (F.J. Rodríquez-Tovar), Javier.Dorador@rhul.ac.uk (J. Dorador), gfrances@uvigo.es (G. Francés), davidcasas@icm.csic.es (D. Casas), thomas.vandorpe@vliz.be (T. Vandorpe), juantomas.vazquez@ieo.es (J.T. Vázquez).

https://doi.org/10.1016/j.margeo.2021.106488
Received 13 November 2020; Received in revised form 9 April 2021; Accepted 9 April 2021
Available online 15 April 2021

circulation (Faugères and Stow, 1993; Howe et al., 1994; Rebesco and Carmelenghi, 2008; Marshall et al., 2014; Ercilla et al., 2016; Juan et al., 2016, among others). A vast scientific community is committed today to the study of these sedimentary archives due to two main reasons. The first is to understand the role of bottom currents in sediment transport/erosion, ultimately contributing to the construction of continental margins (Rebesco et al., 2013, 2014; Marshall et al., 2014; Ercilla et al., 2016; Juan et al., 2016; Miramontes et al., 2016; Rebesco et al., 2016). The second reason is to determine the variability of oceanographic conditions in connection with the climate (Cremer et al., 1993; Revel et al., 1996; Bianchi and McCave, 1999; Stow et al., 2002; Bender et al., 2012; Lebreiro et al., 2018). Contourites provide information on the regional climate (Bianchi et al., 2001; Toucanne et al., 2007; Rogerson et al., 2012) and in some cases, on the global climate as well (Broecker, 1991; Rahmstorf, 2006; Kuhlbrodt et al., 2007), since the bottom currents of oceans are determined by atmospheric forcing.

The information on past ocean circulation and climate changes encoded in contourite drift sediments can be extracted using a wide range of geophysical, sedimentological, paleontological and chemical techniques (Knutz, 2008). In general terms, the use of these techniques provides information at two temporal scales: long ones (millions of years) based on seismic profiles and short ones (thousands of years to centennial variability) based on marine sediment cores. At long timescales, contourite drifts are relatively well distinguished from other sedimentary deposits, such as turbidites and/or instability deposits (Stow and Piper, 1984; Stow et al., 2002; Rebesco et al., 2013; Smillie et al., 2018; Ercilla et al., 2019). At short timescales, significant progress has been made regarding the identification of contourites (Stow et al., 1984, 2002; Faugères and Stow, 1993; Stow and Faugères, 2008; Masson et al., 2010; Bender et al., 2012; Brackenridge et al., 2018; Vandorpe et al., 2019; Stow and Smillie, 2020). But in spite of the progress, identification remains ambiguous and has only been partially resolved (Rebesco et al., 2014) —improved criteria are needed to identify contourites. The difficulties in lithological identification of modern contourites are exacerbated in regions where contourites and downslope deposits are closely interbedded (Stow and Lowell, 1979; Faugères et al., 1984; Shor et al., 1984; Stow and Faugères, 2008; Alonso et al., 2016; Stow and Smillie, 2020), as is the case of the Alboran region in the SW Mediterranean (Fig. 1A). Additionally, several authors have stated that a reliable paleoceanographic signal of contourite drifts at millennial timescales requires the use of multiple sediment cores (Bianchi and McCave, 1999; Bianchi et al., 2001; Petrovid et al., 2019). This approach would allow to detect local and regional variations in the relative strength of bottom currents, and provides a more comprehensive scenarios of circulation regimes and their relationships with the climatic variability. The outflow of warm and highly saline Mediterranean waters into the North Atlantic have played a key role in past within the framework of Northern Hemisphere circulation and global climate. In particular, the Alboran Sea is an area of great interest for paleoclimate/paleoceanography research given its connection with the NE Atlantic through the Strait of Gibraltar, where the saline Mediterranean Outflow Water may significantly affect North Atlantic circulation (Cacho et al., 2001; Combourieu-Nebout et al., 2009; Sánchez-Leal et al., 2017). Ubiquitous Plio-Quaternary contourite drifts, locally interrupted by

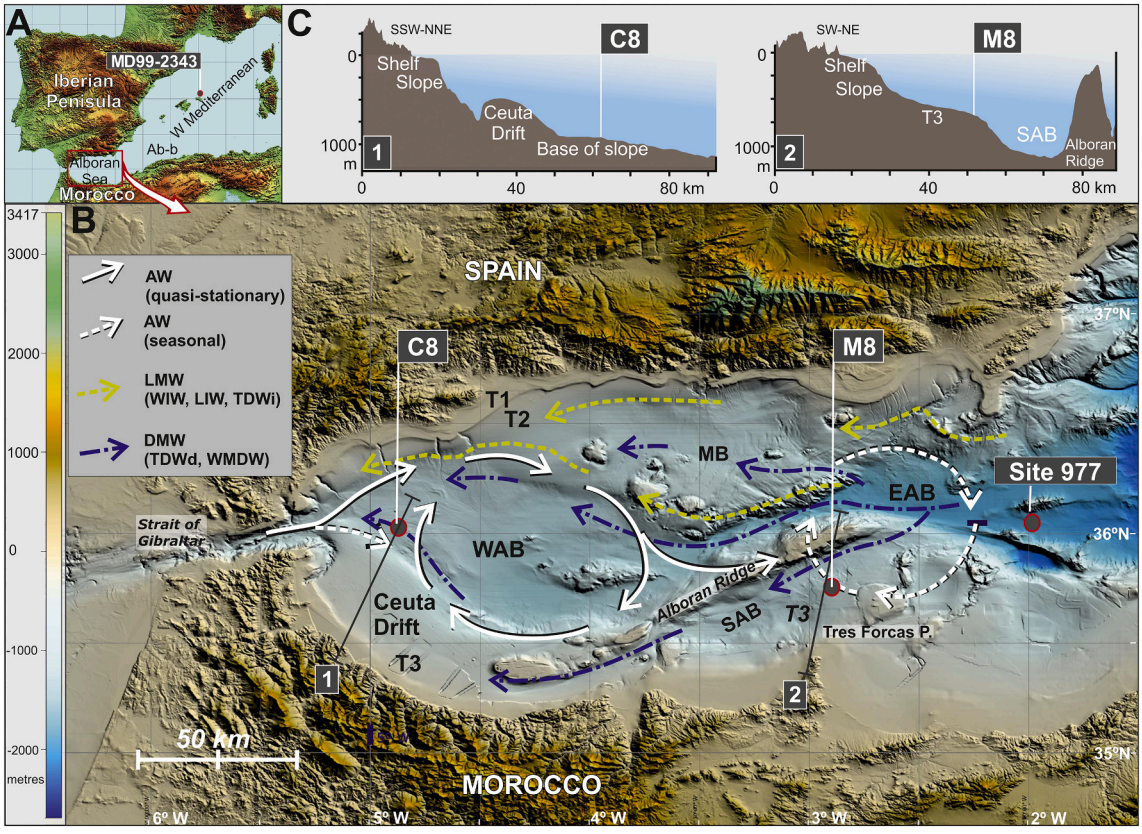

Fig. 1. Location of the sedimentary records used in this study and the main features of oceanic circulation. A) Map of the Western Mediterranean showing the location of the study area and core MD99–2343 addressed in the discussion. B) Bathymetric map of the Alboran Sea indicating the distribution of modern day oceanographic circulation (modified from Ercilla et al., 2016), the location of the two investigated sediment cores (C8 and M8), IODP Site 977, and the place of the two topographic profiles (1 and 2) displayed in Fig. 1C. C) Topographic profiles showing the physiographic location of cores C8 and M8. Legend: AW Atlantic Water, LMW Light Mediterranean Waters (or intermediate), WIW Western Intermediate Water, LIW Levantine Intermediate Water, TDWi upper Tyrrhenian Dense Water, DMW Dense Mediterranean Waters (or deep), TDWd lower Tyrrhenian Dense Water, WMDW Western Mediterranean Deep Water, EAB Eastern Alboran Basin, WAB Western Alboran Basin, SAB South Alboran Basin, MB Motril Basin, T1-T3 contourite terraces, and Ab-b Algero-Balear Basin, P Promontory.

turbidite systems with debris flow deposits, formed owing to intermediate and deep water masses (Ercilla et al., 2016, 2019; Juan et al., 2016, 2020). Together, they provide a comprehensive paleoceanographic scenario from the opening of Gibraltar Strait until the Quaternary (Juan et al., 2016, 2020). The Pliocene circulation favored the redistribution of deep-water masses until the uplift of the Alboran Ridge, and the Quaternary circulation was similar to that at present. In addition, there are indications of a strengthening of the pycnoclines (and hence the density difference between Atlantic and Mediterranean water masses; Juan et al., 2016, 2020). At smaller timescales, the paleo-bottom currents sculpt of these contourite drifts, so their climatic imprint is not well documented (Ercilla et al., 2002; López-González et al., 2019). In contrast, a large dataset of paleoclimate proxies is available for the Alboran Sea, documenting changes in oceanography, productivity, temperature, and redox and wind conditions of both surface and deep water masses at different timescales (Cacho et al., 1999, 2000, 2001; Moreno et al., 2002, 2004, 2005; Colmenero-Hidalgo et al., 2004; Martrat et al., 2004; Rogerson et al., 2005, 2008; Sierro et al., 2005; Jiménez-Espejo et al., 2007; Combourieu-Nebout et al., 2009; Martín-Puertas et al., 2010; Nieto-Moreno et al., 2011; Fink et al., 2013; Rodrigo-Gámiz et al., 2014, 2018; Ausín et al., 2015; Català et al., 2019; Bazzicalupo et al., 2020; among others). Still, certain aspects of the paleoceanographic evolution of the Western Mediterranean Sea over the last 25 cal. kyr BP are not well resolved, *e.g.,* the spatial and temporal quantification of the Western Mediterranean Deep Water (WMDW).

This work presents 25 cal. kyr BP sedimentological and geochemical record of two sediment cores collected in two types of contourite drifts swept at present by the WMDW. The purpose of this work is to: i) determine the high-frequency variations of WMDW paleo-velocities and their relationship with climate variability by compiling an unprecedented high-resolution stratigraphy based on contourite sediments, and ii) to explore the paleoceanographic implications for the Western Mediterranean region.

2. Study area: regional geology and oceanography

The Alboran Sea is the westernmost Mediterranean basin, limited by the Iberian Peninsula (Spanish margin) and North Africa (Moroccan and Algerian margins; Fig. 1A,B). It is a semi-enclosed basin connected to the Atlantic Ocean by the narrow and shallow Strait of Gibraltar in the west and bounded by the Algero-Balearic basin in the East. In turn, the Alboran Sea is composed of four main sub-basins, namely the Eastern, Western, Motril and Southern Alboran basins (Fig. 1B). Each sub-basin has continental margins of complex physiography including intra-slope basins and seamounts. Numerous seasonal steep rivers and streams, all climate-dependant as well characterize the region (Stanley et al., 1975; Liquete et al., 2005; Lobo et al., 2014). On the distal Alboran margins (slope and base of slope) and basins, Plio-Quaternary sedimentation is largely influenced by bottom currents, locally affected by turbidity currents and mass flows (Ercilla et al., 2016; Juan et al., 2016, 2020). Five contourite drift types (plastered, sheeted, elongated and separated, channel-related and mounded confined drifts) dominate the Alboran Sea, each associated with erosive features (moats, channels, terraces and scarps), locally distributed along the margins and basins. The terraces (T1, T2, and T3 in Fig. 1B) extend above large plastered and sheeted drifts showing a combination of proximal erosive and distal depositional characteristics (Juan et al., 2016). They represent extensive flat areas on the upper slope of the Spanish and Moroccan margins (Ercilla et al., 2016). One of the most remarkable contourite features is the Ceuta Drift in the westernmost Moroccan margin (Ercilla et al., 2002; Fig. 1B). Paleoclimate studies of these Alboran deposits shed light on the coupling of oceanographic and atmospheric mechanisms in the Mediterranean region, revealing that this region has been especially sensitive to climatic changes such as the Dansgaard-Oeschger (D/O) and Heinrich Stadials (HSs), implying a strong link between the Mediterranean and North Atlantic climates. Moreover, recent work on Holocene hydro-climatic variability in the Western Mediterranean (Català et al., 2019; Bazzicalupo et al., 2020) demonstrated rapid centennial climate changes, although this period had been considered more climatically stable compared to the previous glacial (Bond et al., 1993; Cacho et al., 1999).

The present-day oceanography at basin scale is dominated by exchange between the Mediterranean Sea and the Atlantic Ocean through the Strait of Gibraltar (Fig. 1A,B). The Alboran Sea is characterized by a thermohaline circulation driven by excessive evaporation with respect to precipitation and runoff (Béthoux, 1979; Macías et al., 2016). At the surface, the Atlantic Water flows eastward, typically forming two (western and eastern) anticyclonic gyres (Fig. 1B; Parrilla et al., 1986; Peliz et al., 2013) and reaching depths of ~150 m in the Spanish margin and ~ 250 m in the Morocco margin. A relatively stable circulation pattern occurs in the western basin, whereas a more variable (seasonal) pattern occurs in the eastern basin. Beneath the surface waters, the Western Intermediate Water (WIW, flowing intermittently along the Spanish upper slope between 75 and 300 m), the Levantine Intermediate Water (LIW, flowing approximately between 200 and 600 m along the Spanish margin and above the adjacent basins) and the upper Tyrrhenian Dense Water (TDWi, which flow together with LIW) comprise the Light Mediterranean Waters (LMW). The lower part of the TDW (TDWd, flowing together with the Western Mediterranean Deep Water) and the Western Mediterranean Deep Water (WMDW, flowing below 400 m on the Spanish margin and deep basins, and below 180 m on the Morocco margin, where the core of the water mass is located, and reaching maximum velocities of 22 cm s^{-1}; Gascard and Richez, 1985; Fabres et al., 2002), comprise the Dense Mediterranean Waters (DMW; Ercilla et al., 2016).

The WMDW flows into the Alboran Sea as three branches (northern, central and southern) locally accelerated by the topography (Millot, 2009). In the Western Alboran basin, the WMDW accelerates due to the effect of the Eastern Alboran gyre and the Bernoulli effect of the Strait of Gibraltar (Fig. 1B; Naranjo et al., 2012; Ercilla et al., 2016). The Western Alboran gyre helps ventilate the WMDW through Strait of Gibraltar, being of key importance for the renewal of the Mediterranean Sea waters (Macías et al., 2016). Despite the Coriolis effect, the main path of the WMDW is the southern one, close to the Moroccan margin, a feature first observed by Bryden and Stommel (1982) using isothermal data. This effect has been further studied and explained by numerical models (Speich et al., 1995; Naranjo et al., 2012).

3. Material and methods

3.1. Sediment cores

Two sediment cores were analyzed, CONT PC8 and MONT PC8 (hereafter called C8 and M8, respectively), whose locations are currently swept by the WMDW (Fig. 1B, C). Core C8 (36°1.22′N and 4°52.3′W) was acquired at 914 m water depth and reaches 648 cm in length. Core M8 (35°46.10′N and 2°52.05′W) was collected at 753 m water depth and reaches 631 cm in length. Core C8 is located within an elongated separated contourite drift, at the base of the Ceuta Drift in the westernmost Moroccan margin (Ercilla et al., 2016). Core M8 is located within a plastered contourite drift, which is part of the outer terrace, called T3 by Ercilla et al. (2016), in the south-central sector of the Alboran Sea (Fig. 1B,C). Both cores were recovered in regions where seismic profiles indicated layered sediments (Juan et al., 2016, 2020), hence relatively undisturbed sedimentary records. Consequently, these cores hold the potential to reveal changes in the strength of this deep-water current. Core C8 was sampled every 2 cm, and core M8 with a 2–6 cm interval and the following analyses were carried out.

3.2. Chronostratigraphic analysis: Stable isotope measurements and AMS ^{14}C

The chronology of core C8 has already been published by Ausín et al. (2015) and is well constrained by fifteen Accelerator Mass Spectrometry (AMS) ^{14}C data. The chronology of core M8 is based on the combination of three AMS ^{14}C data of monospecific samples (*Globigerina bulloides*) and the correlation of the *G. bulloides* oxygen isotopic record ($\delta^{18}O$) with two other records from the Alboran Sea, IODP Site 977 (Martrat et al., 2004) and core C8 (Ausín et al., 2015). The radiocarbon dates were performed at Poznan Radiocarbon Laboratory (Poland) and converted into calendar years (cal. yr BP) using CALIB 7.0.2 software (Stuiver and Reimer, 1993) and the MARINE 13 calibration dataset (Reimer et al., 2013), which allows for comparison of the data with other paleoclimatic records (Table 1). Monospecific samples of planktonic foraminifera *G. bulloides* were handpicked from the >150 μm size-fraction for stable oxygen isotopes analyses ($\delta^{18}O$). The oxygen isotope ($\delta^{18}O$) measurements were carried out by isotope-ratio mass spectrometry (IRMS) in a Finnigan-MAT 252 linked online to a single acid bath Carbon Kiel-II carbonate preparation device at the Scientific and Technological Centres of the University of Barcelona (CCiT-UB). The analytical precision of the laboratory standards was better than 0.08‰ for $\delta^{18}O$, and 0.03‰ for $\delta^{13}C$. Calibration to Vienna Pee Dee Belemnite (VPDB) was performed by means of NBS-19 standards (Coplen, 1996).

3.3. Sedimentological analysis

Terrigenous and carbonate mass accumulation rates (MAR_{terr} and MAR_{bio}) were determined as a potential paleocurrent proxy following Cremer et al. (1993). The MAR of each component (MAR_c, g cm^{-2} ka^{-1}) was calculated from dry-bulk density multiplied by the sedimentation rate (SR) and the proportion of the component fraction (*e.g.,* Kuhn and Diekmann, 2002). The terrigenous clastic percentage content corresponds to the inverse curve of the total $CaCO_3$, subtracting the biogenic opal and total organic carbon component, which is less than 1.5% in all samples (Masqué et al., 2003).

Grain-size analysis was performed on 319 and 160 samples of cores C8 and M8, respectively. These analyses were run on the terrigenous fraction (carbonate free), as it better represents the intensity of bottom currents according to McCave et al. (1995). The terrigenous fraction was obtained by treating the samples with hydrochloric acid to remove the carbonate content. Grain-size analysis was performed using a Coulter LS 100 laser particle size analyzer. The volume % of sand (> 63 μm), silt (4–63 μm) and clay (< 4 μm), and median grain-size (D50) were calculated using the GRADISTAT package (Blott and Pye, 2001). In this study, we used the grain-size standard limits of the Udden-Wentworth grade (Udden, 1914; Wentworth, 1922) in order to describe the sedimentary facies and compare with previous studies (*i.e.,* Stow and Faugères, 2008; Brackenridge et al., 2018). In addition, the mean grain-size of the 10–63 μm terrigenous fraction, known as the sortable silt ($\overline{SS}$), was used as a physical proxy for bottom current (McCave et al., 1995; Bianchi and McCave, 1999; Evans and Hall, 2008; Hoogakker et al., 2011; Lamy et al., 2015; among others) after validating its fidelity. In this case, the $\overline{SS}$ could be used to infer past bottom current velocities based on the calibration of long-term current measurements with $\overline{SS}$ (McCave et al., 2017). This work applies the equation of McCave et al. (2017) for Icelandic overflow (U cm/s = 1.31× $\overline{SS}$-17.18) to estimate paleo-flow velocity change, which has been used in other regions (Roberts et al., 2017; Lebreiro et al., 2018; Spooner et al., 2018). The error was estimated using Coulter Counter, 1.36 ± 0.18 cm s^{-1}/μm (McCave et al., 2017). Some uncertainties of this equation may stem from its calibration for the Icelandic region, and therefore it would represent a semi-quantitative tool for bottom current paleo-velocity reconstructions in the Alboran region.

Composition of the sand fraction was analyzed by binocular microscopy and was conducted on samples of core M8. Terrigenous components were classified as quartz, mica and rock fragments. Biogenic components were classified as planktonic foraminifera (entire and fragments), benthic foraminifera, ostracods, bivalves or gastropods and fossilized faecal pellets. Fossilized faecal pellets were visualized and analyzed by means of Scanning Electron Microscope and X-ray powder to define their shape and nature.

Ichnological analysis was conducted on digital images of core M8 core sections that were previously treated as proposed by Dorador et al. (2014a). This method entails image treatment by modifying certain properties (*i.e.,* levels, brightness and vibrance) to enhance trace fossil visualization (*e.g.,* Dorador et al., 2014b; Rodríguez-Tovar and Dorador, 2015; Dorador and Rodríguez-Tovar, 2018). The analysis was further supported by the use of computed tomography (CT) images taken using a SOMATON definition flash scanner (Vandorpe et al., 2019) and X-Ray images from the Clinic Veterinary Hospital of Universidad Autonoma de Barcelona. CT data was processed using the workflow developed by Dorador et al. (2020) for ichnological analysis of marine sediment cores. Ichno-taxonomical classification of trace fossils was based on the overall shape and the presence of diagnostic criteria such as size and presence of branches (Knaust, 2017).

3.4. Geochemistry analyses

Two chemical element ratios (Zr/Al and Si/(Si + Al) ratios) served to characterize the chemical composition and to interpret oceanographic and environmental changes. The Zr/Al ratio has been previously used as a proxy for bottom currents in other regions (Bahr et al., 2014; Stow et al., 2018) and the Si/(Si + Al) ratio for dry *versus* humid conditions in the Alboran Sea (Moreno et al., 2005; Fink et al., 2013). The relative contents of these elements were measured on split core sediment sections at 1 cm intervals using an Avaatech X-ray fluorescence core scanner at the CORELAB of the University of Barcelona, obtaining higher sampling resolution than with grain-size analysis. A computer-assisted deconvolution process transformed each individual power spectrum into relative contents expressed as counts per second (cps).

3.5. Statistical analysis

3.5.1. Grain-size end-member modelling

To meaningfully identify the sedimentary processes, end-member mixing analysis (EMMA) was applied to the terrigenous grain-size dataset (Weltje, 1997). This statistical tool has applications in many fields of geosciences, and has been successfully used in grain-size studies to identify the imprints of near-bottom currents, turbidity flows and storm floods (Prins et al., 2002; Hamann et al., 2008; Dietze et al., 2014). The numerical statistical algorithm aims to visualize the most significant grain-size changes, explaining variance in the dataset with discrete

Table 1
Results of ^{14}C dating of single planktonic *Globigerina bulloides* taken from core M8.

Core name	This study	Laboratory code	Depth (cm)	Radiocarbon age (years)	Calendar age (cal. years BP)	Cal. kyr
MONT PC 8	M8	Poz-56,250	43–44	3575 ± 35	3492 ± 124	3.5
MONT PC 8	M8	Poz-56,251	321–322	15,630 ± 100	18,506.5 ± 247.5	18.5
MONT PC 8	M8	Poz-56,252	500–501	16,519 ± 160	19,456.5 ± 437.5	19.5

subpopulations, so-called grain-size end-members (EMs, Prins and Weltje, 1999). This technique was applied on the grain-size distribution of the terrigenous fraction of cores C8 and M8, excluding the sandy samples of core C8. Sandy samples of core C8 (n° = 7, from a total n° = 319) were not included in the analysis because they are difficult to assess with EMMA, presenting mostly unimodal distribution of very fine, fine and medium sand that behave as outliers, producing strong deviations in the modelling. The minimal number of EMs to obtain the best approximation of the variance is determined by calculating the coefficient of determination (r^2). The value of r^2 represents the proportion of variance within each grain-size class, which can be reproduced by the approximated data (Weltje, 1997). Afterwards, the relative contribution of each EM may be calculated for every individual particle size distribution. The classical limits of clay and silt mentioned in Section 3.3 have also taken into account for EMMA after Weltje (1997) and Prins and Weltje (1999) to identify discrete grain-size subpopulations.

3.5.2. Spectral analysis

To detect temporal patterns for $\overline{SS}$ and the Zr/Al ratio, both used as potential bottom current proxies, statistical analysis in the frequency domain involved a multivariate Lomb-Scargle periodogram (Scargle, 1982). The Lomb–Scargle periodogram is an effective tool for the study of paleoclimatic/paleoceanographic data (Jiménez-Moreno et al., 2007; Rodríguez-Tovar et al., 2010; Pardo-Igúzquiza and Rodríguez-Tovar, 2011). One aspect that must be considered is the assessment of the statistical significance of the spectral peaks of the estimated smoothed Lomb-Scargle periodogram. This tool evaluates the statistical confidence of the spectral peaks of the estimated power spectrum using the permutation test, enabling differentiation between statistically significant peaks and spurious spectral peaks. Previous research has found that the very high confidence level is usually above 99% and high confidence level is as 70–99% (*i.e.*, Andrews et al., 2003; Rodrigo-Gámiz et al., 2014). This statistical tool was only applied to core C8 for two reasons. First, the results of the spectral analysis depend on the resolution of the power spectrum, conditioned by the number of data available; and second, the most appropriate approach is to work with data at a constant sampling interval (Pardo-Igúzquiza and Rodríguez-Tovar, 2011). As core C8 provided more data (319, *versus* 190 data for M8) and a constant sampling interval (every 2 cm, compared to 2–6 cm for core M8), core C8 would yield results with a higher confidence level.

4. Results

4.1. Age model

The $\delta^{18}O$ record for core M8 follows the general trend of the other well-dated cores, C8 (Ausín et al., 2015) and IODP Site 977 (Martrat et al., 2004), providing additional tie-points for the age model (Fig. 2). It covers the last 25 cal. kyr BP, reflecting the climatic periods MIS 1 (Holocene) and MIS 2. The latter contains the Heinrich Stadial 2 (HS2, period available only in core C8), HS1, the Last Glacial Maximum (LGM) and the Younger Dryas (YD). The last 4.5 cal. kyr BP are only available in the $\delta^{18}O$ record of core M8. The $\delta^{18}O$ values exhibit the typical glacial and Holocene records, with higher $\delta^{18}O$ values during MIS 2 (3.4‰ and 3.54‰ respectively for cores C8 and M8) and lower $\delta^{18}O$ values during the Holocene (−0.093‰ and 0.45‰, respectively for cores C8 and M8, Table S1 in Supplementary data).

4.2. Sedimentation rate (SR) and mass accumulation rate (MAR)

The SR ranges between 11 and 111 cm kyr^{-1} in core C8, and from 14 to 190 cm kyr^{-1} in core M8 (Fig. 3, Table S2 in Supplementary data). According to the average SR and sampling, the resolution is ~65 years for core C8 (Ausín et al., 2015) and ~ 100 years for core M8. In core C8,

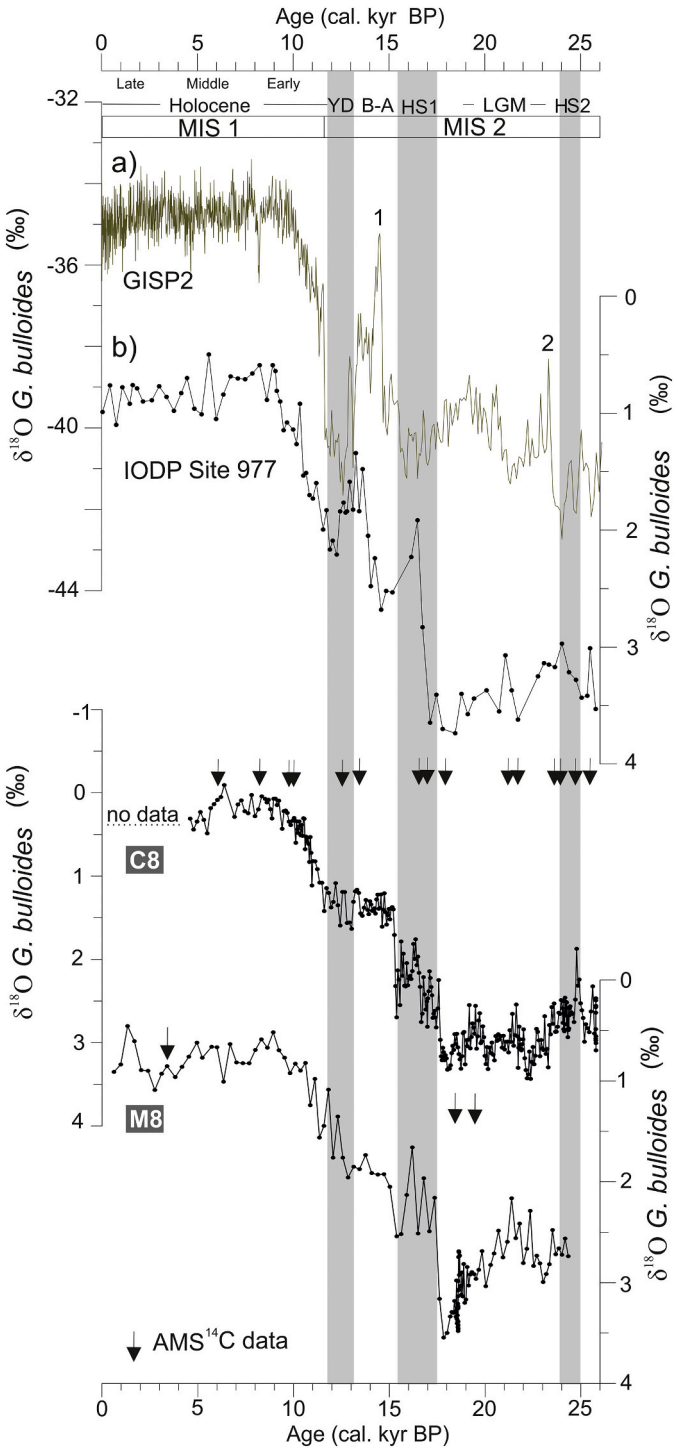

Fig. 2. Oxygen isotopic records ($\delta^{18}O$) for the last 25 ca. kyr BP for the GISP2 ice core (Grootes et al., 1993), IODP Site 977 (Martrat et al., 2004), core C8 (Ausín et al., 2015), and core M8. Black arrows refer to AMS ^{14}C data of cores C8 and M8. The gray bars indicate cold stadials (HS2 Heinrich Stadial 2, HS1 Heinrich Stadial 1, and YD Younger Dryas). LGM Last Glacial Maximum, B-A Bølling-Allerød warm period, MIS 1 and MIS 2 Marine Isotope Stages 1 and 2. Numbers 1 and 2 indicate Dansgaard-Oeschger interstadial events in the GISP2 record.

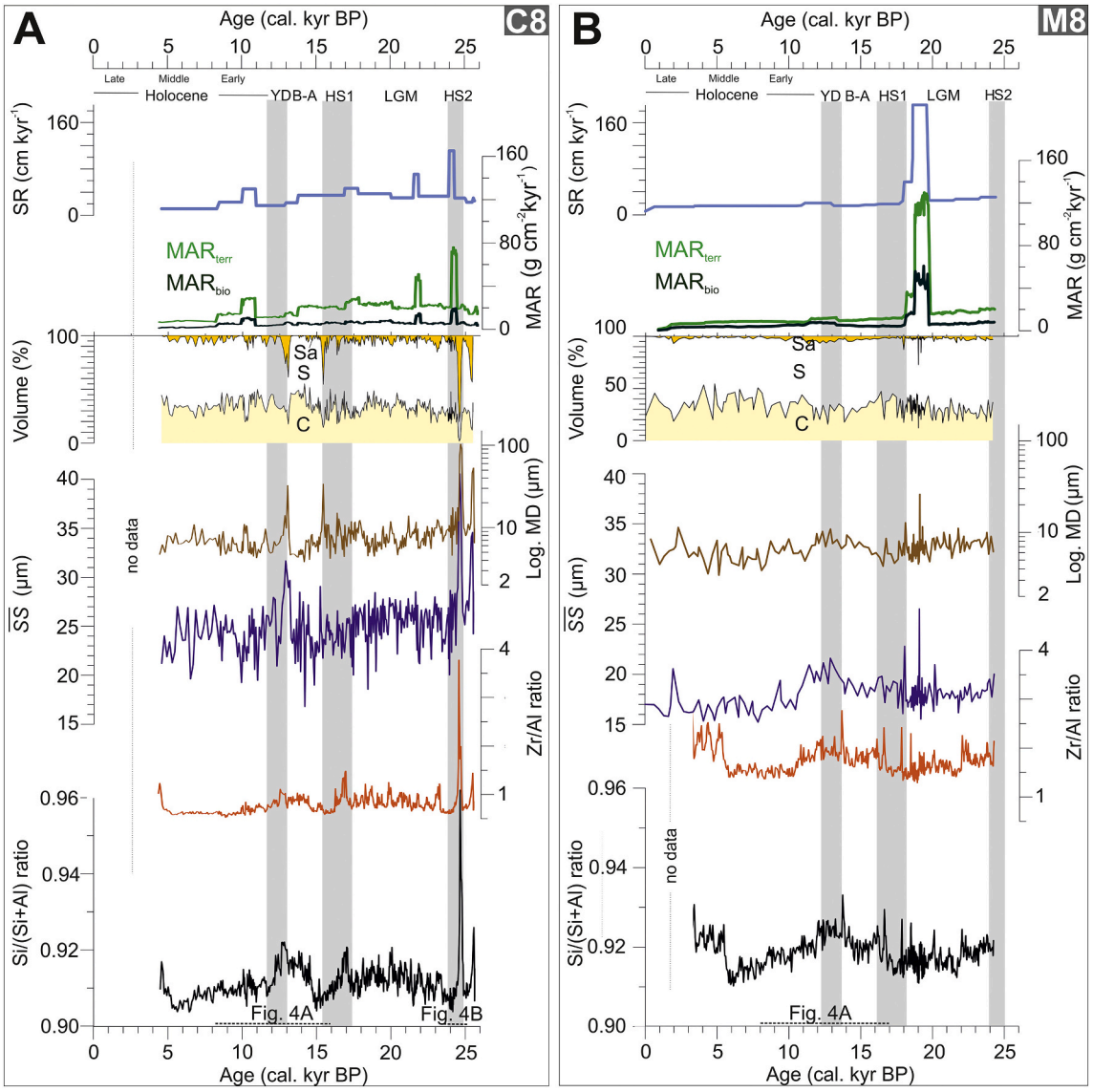

Fig. 3. Sedimentary and chemical characterization of Alboran contourite drifts (cores C8 and M8) based on sedimentation rate (SR), terrigenous and carbonate mass accumulation rates (MAR_{terr} and MAR_{bio}), texture (C Clay, S Silt, and Sa Sand), median grain-size (MD represented in logarithmic scale), sortable silt ($\overline{SS}$), and Zr/Al ratio and Si/(Si + Al) ratio. The gray bars indicate cold stadials (HS2 Heinrich Stadial 2, HS1 Heinrich Stadial 1, and YD Younger Dryas). LGM Last Glacial Maximum, B-A Bølling-Allerød warm period. Dashed lines at bottom refer to temporal windows examined in Fig. 4.

the MAR_{terr} and MAR_{bio} respectively range from 7 to 75 and 1 to 20 g cm^{-2} kyr^{-1} (Fig. 3A, Table S2 in Supplementary data). In core M8, the MAR_{terr} and MAR_{bio} vary from 3 to 129 and 1 to 60 g cm^{-2} kyr^{-1}, respectively (Fig. 3B, Table S2 in Supplementary data). The temporal distribution of both parameters, SR and MAR, show a common overall pattern with high values during the MIS 2 and low values during the MIS 1. A remarkable common feature of MAR is that the MAR_{terr} distribution matches that of MAR_{bio} during the same periods in both cores (Fig. 3). With regard to short-term changes, three maximum peaks are observed in core C8 at HS2 (78 and 20 g cm^{-2} kyr^{-1} of MAR_{terr} and MAR_{bio} respectively), LGM (55 and 17 g cm^{-2} kyr^{-1} of MAR_{terr} and MAR_{bio} respectively), and the early Holocene (30 and 10 g cm^{-2} kyr^{-1} of MAR_{terr} and MAR_{biog} respectively; Fig. 3A). In core M8, only one noticeable maximum peak is recorded, at the interval between 19.5 cal. kyr BP and 18.5 cal. kyr BP (120 and 47 g cm^{-2} kyr^{-1} of MAR_{terr} and MAR_{bio} respectively; Fig. 3B).

4.3. Sedimentological and geochemical characteristics

Four sediment types are identified in cores C8 and M8: (1) *Silty clay*, the finest-grained type (< 8 µm median grain-size), with low sand content (< 5%); (2) *Clayey silt*, which reaches up to 80% silt, has a median grain-size of 7 to 15 µm and low sand content (< 6%) and occurs as several centimeter-sized intervals (1–2 cm); (3) *Sandy silt*, reaches up to 55 µm median grain-size and occurs as several centimeter-sized intervals (< 2 cm, fewer occurrences than type 2); and (4) *Sand*, which reaches up to 80% sand, has a median grain-size of 70 to103 µm (Figs. 3, 4). Core C8 is composed of coarser sediments with higher median grain-size values (4–34 µm) compared to core M8, which shows lower median grain-size values (3.4–13 µm, one sample with 26 µm at 19 cal. kyr BP) for the last 25 cal. kyr BP (Fig. 3, Table S3 in Supplementary data).

In terms of sediment types, both cores contain mainly silty clay with thin and frequent intercalations of silty sediment layers (clayey silt and sandy silt), except for a single thin layer (4 cm) made up of fine sand (up to 103 µm median grain-size) at HS2 (Figs. 3A, 4, Table S3 in Supplementary data). The $\overline{SS}$ absolute values, in turn, range between 17 and

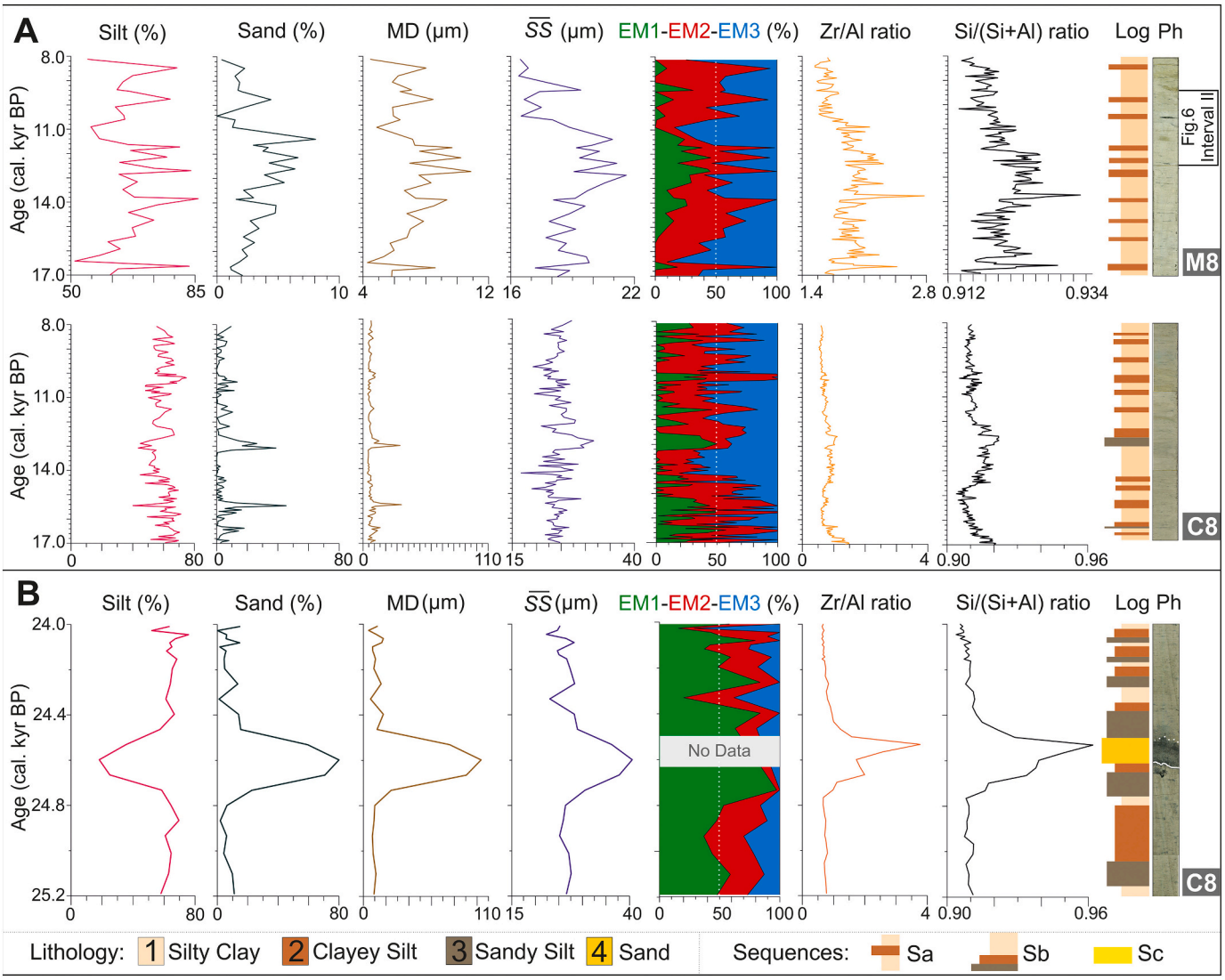

Fig. 4. Two selected time windows, 17–8 cal. kyr BP (A, cores M8 and C8) and 25.2–24 cal. kyr BP (B, core C8), to illustrate in detail the temporal variations of sedimentary parameters (% silt and % sand, MD median grain-size, $\overline{SS}$ sortable silt, EM1 sandy silt, EM2 clayey silt, and EM3 silty clay), chemical proxies (Zr/Al and Si/(Si + Al) ratios), the sedimentary log indicating sequences (Seq) and core photo (Ph) during YD and HS2. Legend: Sa, Sb and Sc refer to the three sedimentary sequences defined in the text. Note the different scale used for core M8.

31.8 μm for core C8, with a single layer that attains 41 μm (HS2); and from 15.2 to 23 μm for core M8 (Figs. 3, 5, Table S3 in Supplementary data). The general trend of $\overline{SS}$ records of cores C8 and M8 displays an overall similar pattern, and document many short, abrupt oscillations (Fig. 5). Forty-five peaks of $\overline{SS}$ are identified in core C8 (Fig. 5b) and are denoted as e4-e53, where "e" refers for the elongated separated contourite drift. Forty peaks of $\overline{SS}$ in core M8 (Fig. 5d) are indicated as p1-p50, where "p" refers to the plastered contourite drift. They are ordered from younger to older; the number signals age, so that equal numbers imply contemporary peaks of $\overline{SS}$ at both cores (*e.g.,* e23 and p23 at YD; Fig. 5b,d). Most of them coincide with high values in $\delta^{18}O$ (Fig. 5a). Five maximum peaks of $\overline{SS}$ are identified in core C8 (Fig. 5b), occurring at HS2-peak e52 (up to 41 μm), LGM-peak e44 (up to 28.5 μm), 18.9 cal. kyr BP-peak e35 (up to 28.5 μm), 15.2 cal. kyr BP-peak e27 (up to 29 μm) and YD-peak e23 (up to 31.8 μm). Four maximum peaks of $\overline{SS}$ are identified in core M8 (Fig. 5d), two found at LGM-peaks p39/p33 (up to 21/22.8 μm, respectively), YD-peak p23 (up to 21.6 μm), and late Holocene-peak p1 (up to 20.8 μm).

The temporal distribution of the Zr/Al and Si/(Si + Al) ratios of cores C8 and M8 shows a general common trend (Fig. 3). This trend follows the pattern of $\overline{SS}$ with the highest peaks at HS2, LGM, HS1, and YD (Fig. 3, Table S4 in Supplementary data). The sand fraction studied in core M8 is mainly composed of bioclasts with abundant bivalve fragmented shells and foraminifera, mixed with terrigenous components (*e.g.,* rock fragments, micas; Fig. 6A i-ii). The faunal content largely consists of planktonic and benthonic foraminifera, and the state of preservation is good. A remarkable component is the high presence of faecal pellets (Fig. 6A iii-iv). They may constitute up to 20% of the sand fraction. The faecal pellets display tubular and spherical shapes with rounded edges and irregular surfaces. Chemical XRD analyses indicate that these pellets are mainly a mixture of quartz and calcite, some having high values for sulfur (see Fig. S1 in Section 2 of Supplementary data).

According to the ichnological features, including ichnofabrics, trace fossil composition, diversity and abundance of traces, three intervals (I, II, and III, from younger to older) can be discerned along core M8 (Fig. 6B). Interval I corresponds to the last deglaciation and Holocene periods. It is characterized by a well-developed mottled background and a comparatively scarce record of discrete trace fossils. Fossil assemblages are dominated by *Planolites* and *Palaeophycus*, with very rare

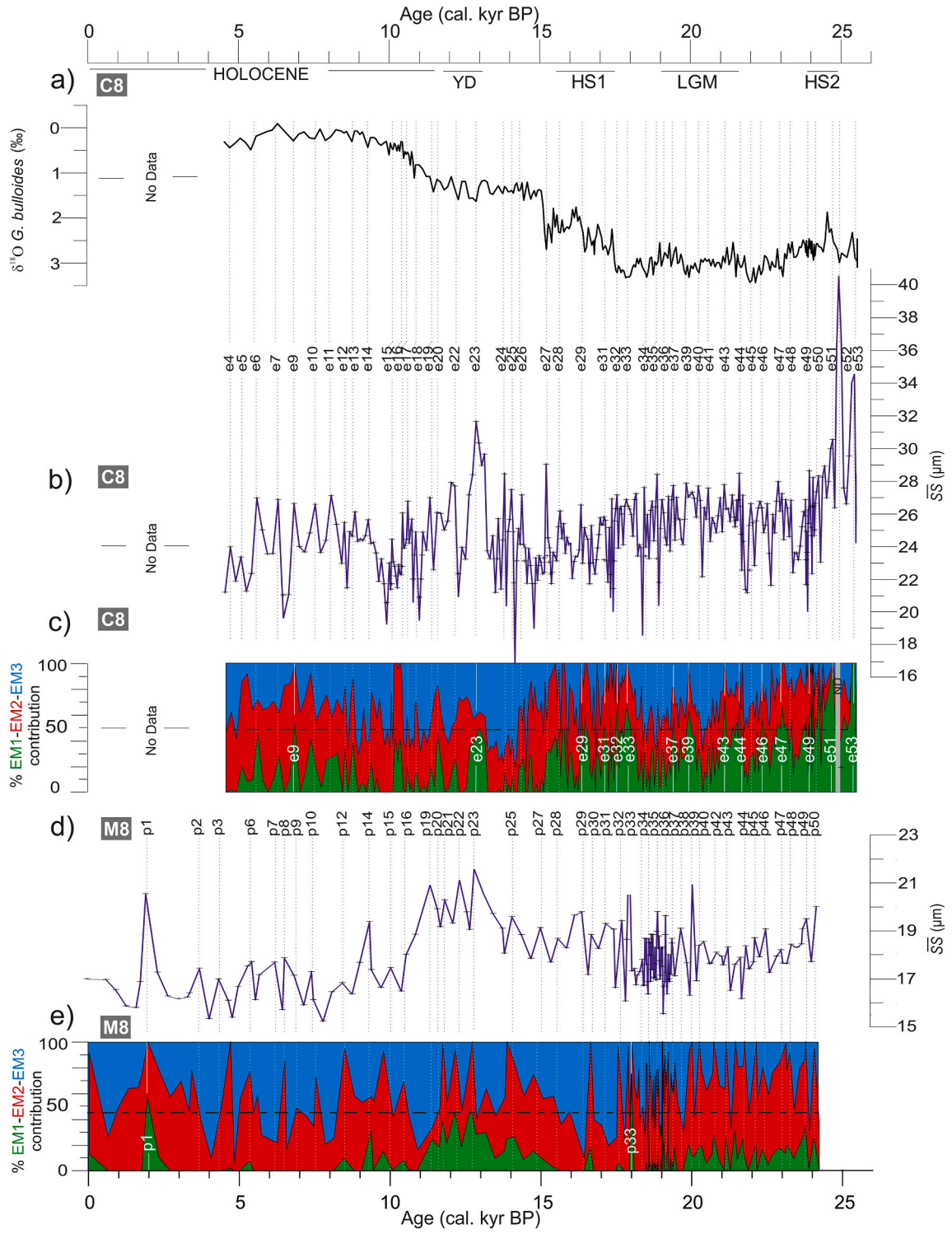

Fig. 5. Silty layers named e4-e53 (from younger to older) of the elongated separated contourite drift (C8) and p1-p50 (younger to older) of the plastered contourite drift (M8) for the past last 25 cal. kyr BP: a) oxygen isotope record ($\delta^{18}O$) of core C8, b) $\overline{SS}$ record of core C8, c) EM1-EM2-EM3 contributions of core C8, d) $\overline{SS}$ record of core M8, and e) EM1-EM2-EM3 contributions of core M8. Solid white line in the EM graphs c) and e) refer to sandy silt layers. Legend: $\overline{SS}$ Sortable silt, ND no data, HS2 Heinrich Stadial 2, LGM Last Glacial Maximum, HS1 Heinrich Stadial 1, and YD Younger Dryas.

occurrences of *Thalassinoides* and *Asterosoma*, and occasional vertical structures (Fig. 6B). Interval II developed during most of the deglaciation period. This interval shows a significant change with respect to the previous one. It has a homogeneous background, a more diverse and abundant distinct trace fossil assemblage and more vertical structures *(Teichichnus*, and *Asterosoma*), as well as fewer horizontal traces (*Planolites*, *Palaeophycus, and Phycosiphon)*. Interval III corresponds to the LGM. This interval also shows a significant change with respect the previous one. It is defined by alternate slightly mottled and homogenous backgrounds. Abundant distinct ichnological traces are observed, with a dominance of horizontal structures (*Planolites* and *Palaeophycus*), some of them showing active meniscate fill (?*Taenidium*,?*Scolicia*). Other

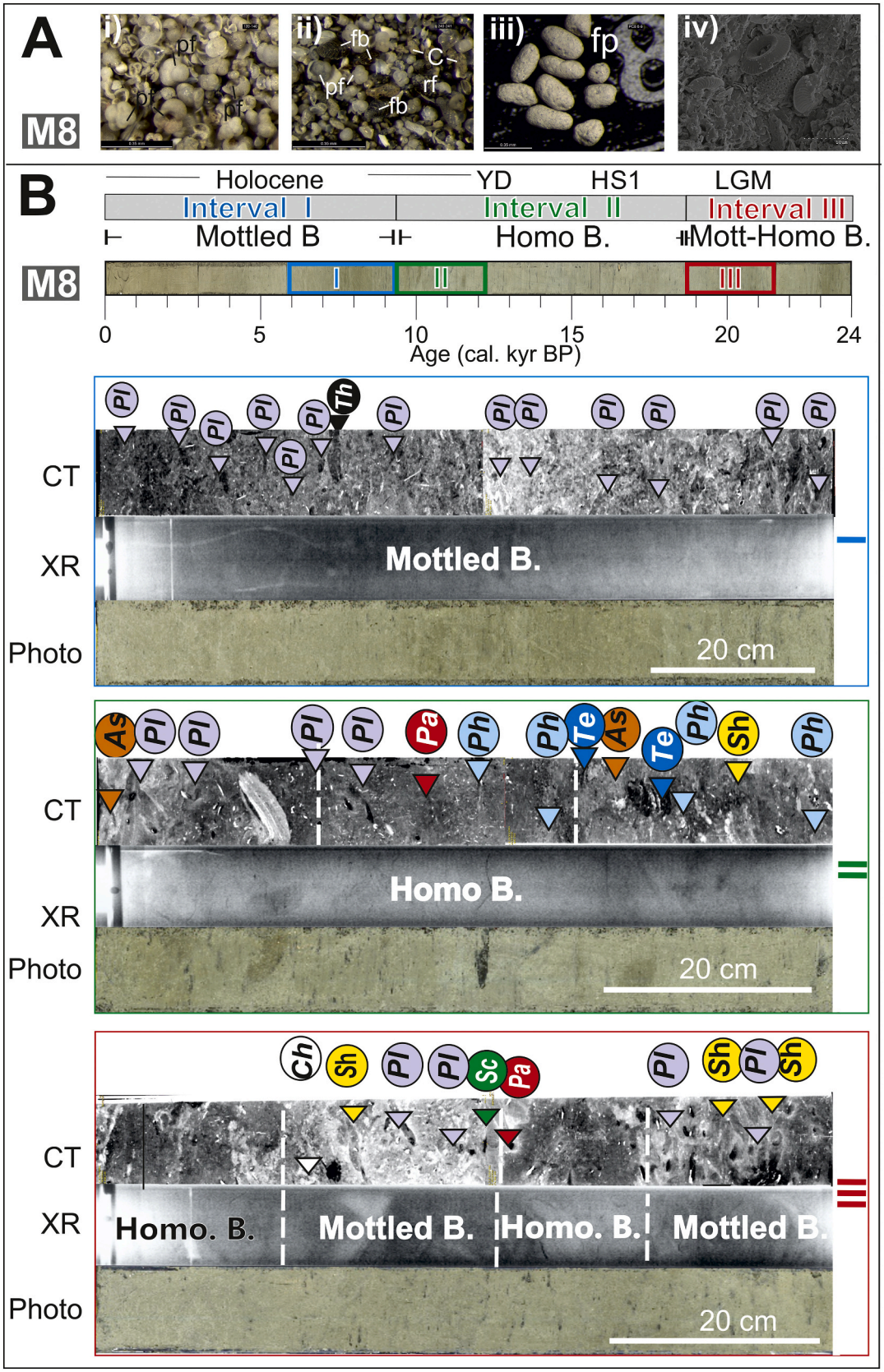

Fig. 6. Main composition of sand fraction and ichnological results of core M8. A) Binocular microscope photo of the sand fraction (i, ii and iii), and microphotograph SEM of faecal pellets (iv). B) Upper panel shows a core photo with three ichnological intervals I, II, and III (younger to older); Lower panel illustrates selected images of computed tomography (CT), X-Ray (XR) and photo showing trace fossil assemblage of these intervals. Legend: pf planktonic forams, bf bentonic forams, fp faecal pellets; *As Asterosoma*, *Ch Chondrites*, *Pa Palaeophycus*, *Ph Phycosiphon*, *Pl Planolites*, *Sc Scolicia*, *Te Teichichnus*, *Th Thalassinoides*, Sh Horizontal spreite structures, Homo Homogeneous, B Background, Mott Mottled, LGM Last Glacial Maximum, HS1 Heinrich Stadial 1 and YD Younger Dryas.

traces as *Chondrites* and *Asterosoma* are identified as well.

4.4. Grain-size end-member modelling

Cores C8 and M8 were investigated separately, as end-member modelling can be influenced by local geological and oceanographic conditions. Three end-members, EM1, EM2, EM3, render respective coefficients of determination of 0.95 and 0.96 for cores C8 and M8. The three EMs differ in their texture, median grain-size and mode grain-size (Fig. 7). In core C8, EM1 is sandy silt, with a median grain-size of 39 μm and a mode grain-size of 47 μm. EM2 is clayey silt with a median grain-size of 8 μm and a mode grain-size of 6 μm. EM3 is silty clay with a median grain-size of 3 μm, a mode grain-size of 3 μm, and two subordinate modes 0.37 and 47 μm (Fig. 7A). In core M8, EM1 is sandy silt with a median grain-size of 28 μm and a mode grain-size of 23 μm. EM2 is clayey silt in nature with a median grain-size of 7 μm and mode grain-size of 12 μm. EM3 represents the finest sediments with the same median and modal grain-sizes as EM3 of core C8 (Fig. 7B). These statistical grain-size results allow one to summarize that EM1 has the nature of sandy silt, EM3 of silty clay (finest-grained particles); in between them, the EM2 is characterized by clayey silt. The temporal distribution of the silty layers (EM1 and EM2) is different in the two cores (Fig. 5c, e). Whereas they are mainly clayey silt layers for the Holocene (e4-e19), with a low contribution of EM1 (< 45%), the MIS 2 is dominated by sandy silt layers with EM1 > 45%, in particular during climate periods HS2, LGM, HS1 and YD, where the respective values reach 82%, 70%, 63% and 50% (Fig. 5c, Table S5 in Supplementary data). Even though core M8 shows predominantly clayey silt layers (low contribution of EM1 < 45%) throughout the MIS 2 and Holocene, it also contains just two sandy silt layers named p33 (LGM) and p1 (late Holocene), where EM1 contributes as much as 73 and 58%, respectively (Fig. 5e).

4.5. Spectral analysis

In core C8, the spectral analysis of $\overline{SS}$ displays a remarkable cycle of ~ 2300 yr (peak 2292 yr) with up to 97% confidence level significance (CL; Fig. 8A). Spectral analysis of the Zr/Al ratio displays four cycles, of ~1900 yr (peak at 1912), ~ 2300 yr (peak at 2312 yr), ~ 4000 yr (peak at 3975 yr), and ~ 6200 yr (peak at 6200 yr) with high and very high CL (93 to 99%; Fig. 8B). These peaks having high and very high CL are considered as primary, and interpreted in our discussion. Notwithstanding, the spectral analysis of these proxies displays further peaks at low frequencies, registered close to the vertical axis of the CL and calibrated as higher than 7000 yr. They are not considered according to Rodrigo-Gámiz et al. (2014), who hold that cycles at the lowest frequencies could be a consequence of spectral analysis involving core spans around 25 cal. kyr BP.

4.6. Vertical succession of the lithology: sedimentary sequences

The gradual lithology succession along cores C8 and M8 makes it possible to identify three sequences, Sa, Sb, and Sc (Fig. 4). Both Sa and Sb consist of fine-grained sediments (3–39 μm median grain-size) and were deposited over the last 25 cal. kyr BP (Figs. 4A, 9A). Sa is defined by the vertical succession of silty clay, clayey silt, and again silty clay, which is represented by the vertical succession of EM3, EM2, EM3 (lithology 1, 2, 1; Fig. 4A in core M8). Sb comprises the vertical succession of sandy silt, clayey silt, and silty clay pertaining to EM1, EM2, and EM3 (Fig. 4A in core C8). The contacts are gradational through vertical lithological succession within sequences Sa and Sb (Fig. 4A). In turn, sequence Sc, with sharp boundaries, consists of sand (up to 103 μm median grain-size; Fig. 4B) representing a coarse-grained sequence, not enclosed for end-member modelling; it was deposited during HS2 (Fig. 4B). Most of the maximum grain-size values of these three sequences match high peaks of the $\overline{SS}$ and Zr/Al and Si/(Si + Al) ratios (Fig. 4).

5. Discussion

5.1. Defining the WMDW influence in the Alboran contourite drifts over the last 25 ca. kyr BP

The comparable patterns displayed by both cores, C8 and M8, in terms of $\overline{SS}$ (Fig. 5b,d) as well as the $\overline{SS}$ *vs* Zr/Al ratio (Fig. 4), in addition to the remarkable similarity between MAR_{terr} and MAR_{bio} records (Fig. 3), suggest that the biogenic carbonates are transported, deposited and reworked by bottom currents similarly to the terrigenous material. So that the defined sequences (Sa, Sb, Sc) making up both contourite drifts (plastered and elongated separated) would have been formed under the action of a similar bottom layer, despite their different

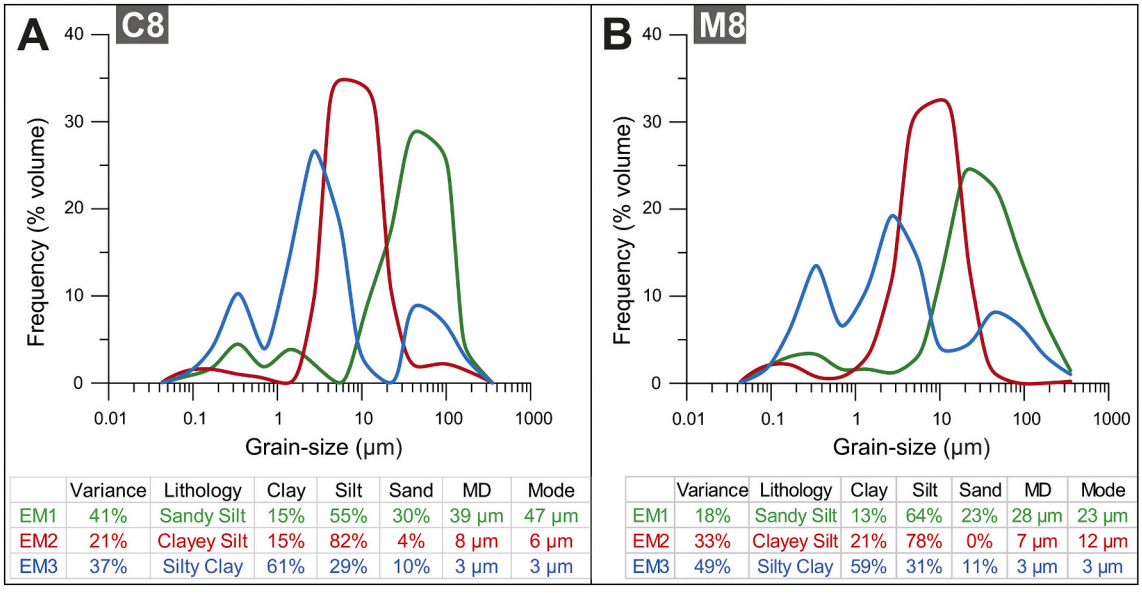

	Variance	Lithology	Clay	Silt	Sand	MD	Mode
EM1	41%	Sandy Silt	15%	55%	30%	39 μm	47 μm
EM2	21%	Clayey Silt	15%	82%	4%	8 μm	6 μm
EM3	37%	Silty Clay	61%	29%	10%	3 μm	3 μm

	Variance	Lithology	Clay	Silt	Sand	MD	Mode
EM1	18%	Sandy Silt	13%	64%	23%	28 μm	23 μm
EM2	33%	Clayey Silt	21%	78%	0%	7 μm	12 μm
EM3	49%	Silty Clay	59%	31%	11%	3 μm	3 μm

Fig. 7. Grain-size end-member modelling results of the cores C8 (A) and M8 (B) showing the grain-size distribution of the three EMs (EM1-EM2-EM3) indicating variance, lithology, texture (clay, silt, and sand), median grain-size (MD), and mode grain-size.

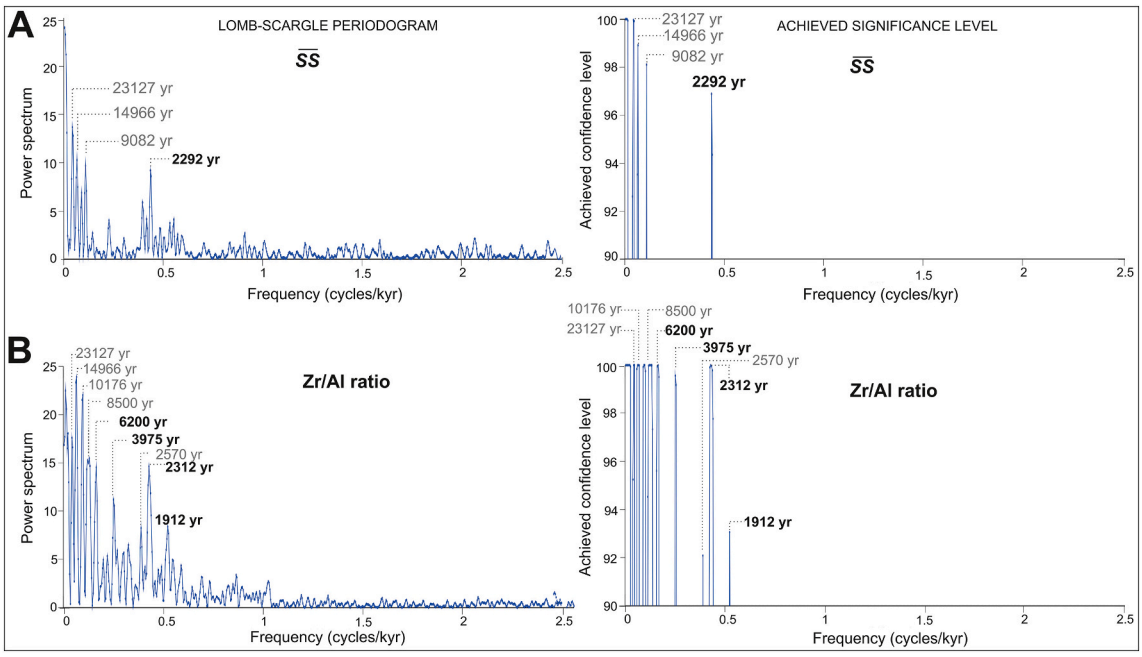

Fig. 8. Spectral analysis of physical ($\overline{SS}$) and chemical (Zr/Al ratio) bottom current proxies from core C8. A) Sortable silt ($\overline{SS}$) and B) Zr/Al ratio. Spectral peaks registered with Lomb-Scargle periodogram and their achieved confidence levels, shown on the left and right, respectively. Black numbers refer to the peaks interpreted in this work. Gray numbers refer to peaks not considered in this work.

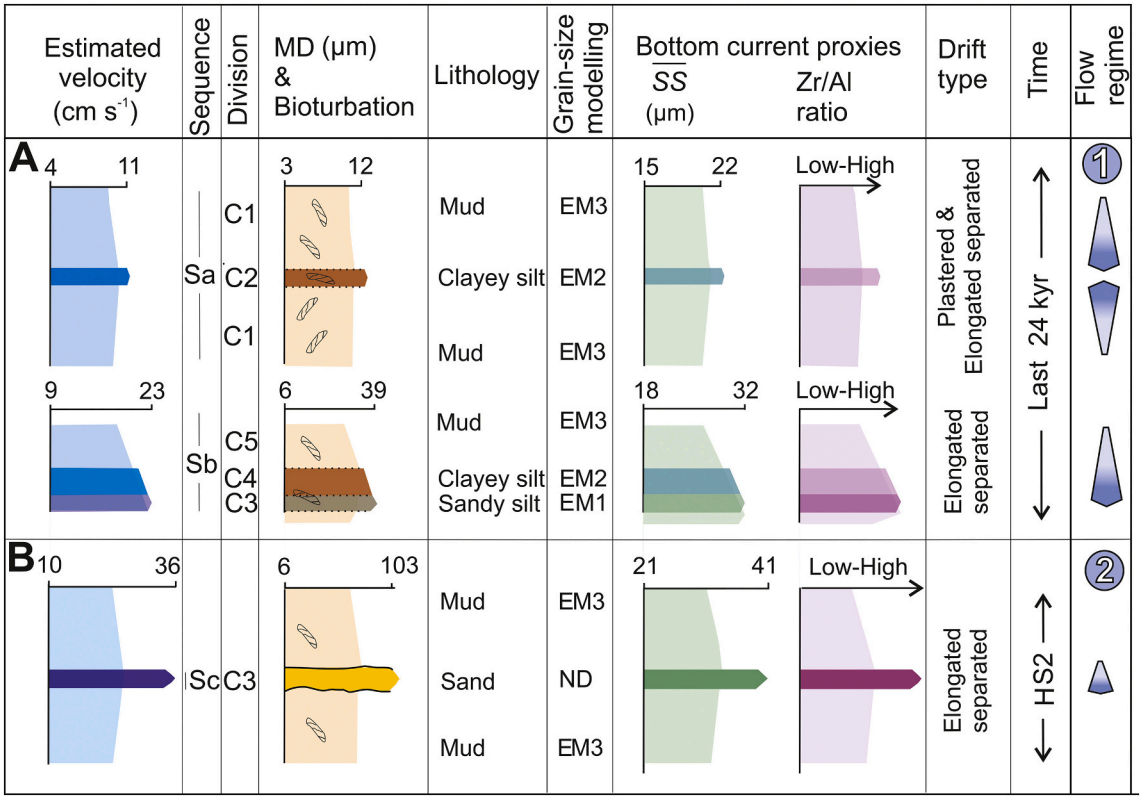

Fig. 9. Two flow regimes of WMDW and key characteristics for the last 25 cal. kyr BP: flow regime 1-weak to moderate paleo-velocities (2–23 cm s^{-1}) represented by sequences Sa and Sb; and flow regime 2-stronger paleo-velocities (up to 36 cm s^{-1}). C1 to C5 refer to generic contourite divisions defined by Stow and Faugères (2008). Legend: MD Median grain-size, and ND no data.

geographic locations (Spanish and Morocco margins; Fig. 1B,C). As a consequence, the role of alongslope processes in the terrigenous grain-size distribution is demonstrated. The sediment source could be considered as a secondary control on grain-size distribution when sediments from the continent reach the sea they are quickly dispersed and distributed by the Atlantic and Mediterranean waters (Ercilla et al., 2016). Based on the present day Mediterranean water mass circulation (Ercilla et al., 2016) and paleoceanography (Juan et al., 2016, 2020), this bottom layer corresponds to WMDW. The vertical succession of lithology within sequences Sa and Sb is respectively represented by EM3-EM2-EM3 and EM1-EM2-EM3 (Fig. 9A), which could be equivalent to the generic contourite divisions defined by Stow and Faugères (2008). The sequences Sa and Sb could represent divisions C1–2 (or C4–5) and C2–3-4, respectively, corresponding to base cut-out sequences (Fig. 9A). The repeated coarsening and fining upward grain-size trends of finer-grained sequences, documented in muddy contourite successions worldwide, point to an increase and then decrease of bottom current competency, from weak to strong, to weak again (Toucanne et al., 2007; Stow and Faugères, 2008; Rebesco et al., 2014; Brackenridge et al., 2018; Stow et al., 2018). The sequence Sc could mark the contourite division C3 (Fig. 9B). Indeed, grain-size variations show periodic increases and decreases, as described in Stow et al. (2018), for which reason their periodicity was evaluated by spectral analysis (see Section 5.3).

5.2. Alboran Sea paleoceanography

5.2.1. WMDW paleo-velocities: flow regimes

Up to now, no quantifications of WMDW flow paleo-velocities deriving from contourite sequences have been documented for the Alboran Sea, or the entire Mediterranean Sea for that matter. Estimations of flow velocity changes inferred from $\overline{SS}$ were obtained by applying the equation for Icelandic overflow (U cm/s = 1.31×$\overline{SS}$-17.18; McCave et al., 2017). This equation served to distinguish two regimes in terms of WMDW flow energy: 1) weak to moderate velocities (~4–23 cm s^{-1}) represented by sequences Sa and Sb; and 2) stronger velocities (up to ~36 cm s^{-1}) represented by sequence Sc (Fig. 9).

Regime 1-Weak to moderate velocity. This regime has prevailed on the Alboran contourite drifts during the last 24 cal. kyr BP (Fig. 9A). The bottom current paleo-velocity is estimated to be between ~4 and 23 cm s^{-1} (Fig. 9A, cores C8 and M8 in Table 2). Sequences Sa (equivalent to C1–2 or C4–5) and Sb (equivalent to C3–5) would have been deposited in this regime. Regime 1 implies alternate periods of weak and moderate flow velocities. Sequence Sa was deposited under relatively weak bottom current velocities, between ~4 and 11 cm s^{-1}, while sequence Sb was deposited under moderate flow velocity, reaching up to ~23 cm s^{-1} (Fig. 9A). These velocities agree with those of the general contourite facies model (Faugères and Mulder, 2011), from 5 to 10 cm s^{-1} at the base (fine-grained part of sequence) and 18 to 25 cm s^{-1} in the middle part (coarse-grained part of the sequence). The range of flow velocity estimations (~4–23 cm s^{-1}) for the Alboran muddy contourites is consistent with Stow et al. (2002), who determined an average paleo-velocity of 10–20 cm s^{-1} for muddy contourites; and with Lebreiro et al. (2018), who estimated paleo-velocities around 16 cm s^{-1} for silty contourites in the Gulf of Cadiz under the action of the Mediterranean Outflow.

Theoretically, the weak to moderate energy of bottom currents linked to sequence Sa should be characterized by variations in both abundance and composition of ichnofabric and trace fossil assemblages (Rodríguez-Tovar et al., 2019a, 2019b, 2019c). This can be observed in the sequence Sa of core M8 (Fig. 6B). The dominant presence of horizontal structures containing nearly exclusive *Planolites* and *Palaeophycus* and only occasional vertical structures in the mottled background would suggest a low rate of sedimentation (backed up by the calculated values of <15 cm kyr^{-1}; Fig. 3B), supporting weaker bottom currents during the Holocene (MIS 1). On the other hand, the abundant vertical spreiten structures *Teichichnus* and *Asterosoma* observed during short periods, as the LGM and the YD, suggest a significant increase in the rate of deposition, impeding complete bioturbation of the seafloor during a period of increased bottom currents (Dorador et al., 2019).

Furthermore, the estimated paleo-velocities of sequences Sa and Sb are coherent with moored array measurements at comparable depths (971 m) of core C8 (915 m) in the Western Alboran Sea, averaging values of 2–5 cm s^{-1} with maximum peaks of 22.3 cm s^{-1} (Fabres et al., 2002; Sanchez-Vidal et al., 2005). Additional mooring measurements at 770 m water depth (35°41.61′N and 3°0.9′W), 27 km ESE of core M8, indicated low average velocities (one-year average of 1 cm s^{-1}; Vargas-Yáñez et al., 2002). The estimations based on grain-size data seem coherent with nearby recorded data, but unfortunately, no direct measurements are available for the precise locations of the studied cores.

Regime 2- Stronger velocity. This regime occurs only during HS2 in core C8 (Fig. 9B). It is characterized by estimated paleo-velocities of about ~36 cm s^{-1}, that is, 1.5 to 3 times higher than the velocities of regime 1. This estimated velocity is within the range required to move quartz sand, which would take 35–37 cm s^{-1} (McCave, 2008). Sequence Sc, displaying sharp erosive boundaries (Fig. 4B), was deposited during this regime. Its sandy sediments, equivalent to division C3 (Fig. 9B), may represent erosional or residual sediments deposited during an elevated bottom current regime. The sequence marks an erosive episode, characterized by sandy contourites deposited directly a top older contourite muds (Fig. 4B). A sudden and strong change in bottom current velocity is inferred. This sequence type was likewise documented in mounded contourite drifts in the Cadiz Depositional System (Brackenridge et al., 2018). Because only the middle sandy division is preserved, the sequence was referred to as "mid-only contourites" by Stoker et al. (1998). They could easily be confused with thin-bedded sandy turbidites, although the pervasive bioturbation, the similar pattern of MAR_{terr} and MAR_{bio}, the correlation of bottom current proxies ($\overline{SS}$ and Zr/Al ratio) with arid proxy Si/(Si + Al) ratio (Fig. 3A), and the lack of any normal grading are sound criteria used to discriminate them. As "mid-

Table 2
WMDW flow estimated paleo-velocity (cm s^{-1}) for the last 24 cal. kyr BP representing flow regime 1 (weak to moderate velocity). Legend: "a" and "d" refer to acceleration and deceleration sub-phases identified in Figure 10A, FCE Fast Current Events.

Phase	acceleration/	FCE	Sortable Silt & Estimation of bottom current paleo-velocity					
	decceleration		MD99–2343		C8		M8	
	(a/d)		NW Mediterranean		SW Mediterranean		SW Mediterranean	
I	Ia	FCE-I	26.7 μm	~18 cm s^{-1}	28 μm	~19 cm s^{-1}	20 μm	~9 cm s^{-1}
	Id		24.0 μm	~14 cm s^{-1}	23.2 μm	~13 cm s^{-1}	17.2 μm	~5 cm s^{-1}
II	IIa	FCE-II	26.7 μm	~17 cm s^{-1}	26.7 μm	~17 cm s^{-1}	19.8 μm	~9 cm s^{-1}
	IIa		20.3 μm	~9 cm s^{-1}	22.2 μm	~12 cm s^{-1}	18 μm	~6 cm s^{-1}
III	IIIa	FCE-III	24.5 μm	~15 cm s^{-1}	31 μm	~23 cm s^{-1}	21.2 μm	~11 cm s^{-1}
	IIId		16.5 μm	~4 cm s^{-1}	20.5 μm	~9 cm s^{-1}	16.7 μm	~4 cm s^{-1}
IV	IVa	FCE-IV	25.2 μm	~16 cm s^{-1}	26.2 μm	~17 cm s^{-1}	17.7 μm	~6 cm s^{-1}
IV	IVd		18.9 μm	~8 cm s^{-1}	22.9 μm	~9 cm s^{-1}	16.2 μm	~4 cm s^{-1}

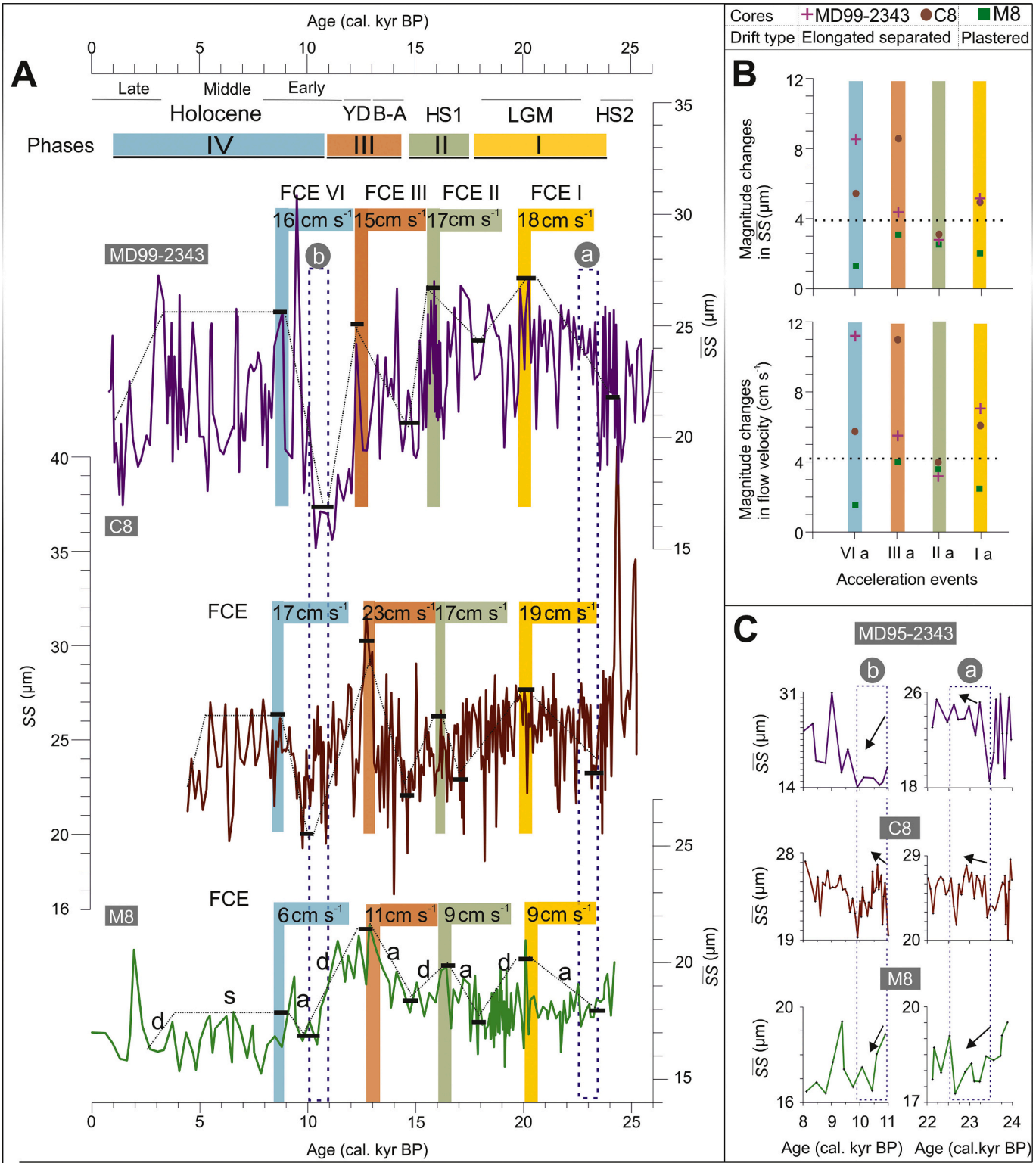

Fig. 10. Millennial scale dynamics of WMDW flow for the last 24 cal. kyr BP from the NW (core MD99–2343) to SW Mediterranean (cores C8 and M8). A) Temporal distribution of the three $\overline{SS}$ records showing four synchronous phases (I to IV) indicating accelerations (a), deceleration (d) and steady (s) subphases and estimated paleo-velocities of the fast current events (FCE). B) Two binary plots represented by the magnitude change in $\overline{SS}$ and in WMDW flow paleo-velocity *vs* the four current acceleration subphases (Ia to IVa). C) Temporal distribution of $\overline{SS}$ for two temporal windows, 23.5–22.5 and 11–10 cal. kyr BP showing two non-synchronous events of the WMDW.

only contourites" are most likely preserved in certain ancient sequences, the description of this type in modern environments —such as the Alboran drifts of this study— may have implications for the delineation of contourites in ancient successions.

5.2.2. Local variability of the WMDW paleo-flow velocity

When comparing the WMDW paleo-velocities inferred from cores C8 and M8, some noteworthy differences are observed for the last 24 cal. kyr BP (Figs. 9A, 10, Table 2). The plastered contourite drift (core M8), composed by finer-grained contourites (< 13 μm median grain-size, one sample with 28 μm; Fig. 3B) with low SR (mostly below 20 cm kyr^{-1}) and MAR_{terr} (mostly below 20 g cm^{-2} kyr^{-1}; Fig. 3B), was formed under slow flow velocities (~ 4 to 11 cm s^{-1}; Fig. 9A). It displays minor magnitude changes in flow velocity (1.5–4 cm s^{-1}; Fig. 10B). To the contrary, the elongated separated contourite drift (core C8) defined by coarser-grained contourites (below 39 μm median grain-size; Fig. 4A), and high SR (mostly below 45 cm kyr^{-1}) and MAR_{terr} (mostly below 30 g cm^{-2} kyr^{-1}; Fig. 3A), was deposited under enhanced flow velocities (~9 to 23 cm s^{1}, Table 2). It records major magnitude changes in flow velocity (~4–11 cm s^{-1}; Fig. 10B). These differences are probably related to the local hydrodynamic and morphological contexts surrounding the cores´ retrieval, suggesting that the WMDW paleo-velocity changes along its route (Fig. 1B). Indeed, the stronger hydrodynamic regime defined for the core C8 is linked to the local acceleration of the WMDW during the Quaternary due to interplay between the nearby Strait of Gibraltar and the morphological constraint of the Ceuta Drift (Fig. 1B; Ercilla et al., 2019; Juan et al., 2020). In contrast, the weaker hydrodynamic regime estimated for core M8, deposited in open slope conditions, agrees with the weak currents recorded in modern oceanographic measurements close to this core (1 cm s^{-1} average; Vargas-Yáñez et al., 2002). The abundant presence of faecal pellets (Fig. 6A) within sequence Sa of core M8 also supports a weak bottom current. The preservation of such components in the sedimentary record, attributed to the activity of small crustacean (*e.g.,* crab, L. Cross Pers. Commun., 2020), points to low energetic environments on the seafloor. This hypothesis is supported by the minor variations in magnitude changes of WMDW velocity (1.5 to 4 cm s^{-1}; Fig. 10B), as well as the weak paleo-velocities estimated for core M8 (~4–11 cm s^{-1}; Fig. 9A, Table 2). In addition, the presence of sulfur-bearing discrete trace fossils throughout the sedimentary record of core M8 (see Fig. S1 in Supplementary data) suggests low-oxygen conditions most likely related to poorly ventilated bottom waters due to weak bottom currents (Wetzel, 1984).

5.3. Paleoclimatic implications. Contourite cyclicity of millennial scale variability and forcing mechanisms

Variations in contourite characteristics —with the alternation of coarser- and finer-grained contourites, hence changes in the nature of contourite deposition— appear to be the norm at all scales of observation (seismic profiles and sediment cores; Stow et al., 2018). The Alboran contourite successions, formed mainly by the alternation of silty and muddy deposits, also display cyclicity (Figs. 4, 5). Visual analysis of the sedimentological logs (Fig. 4A) points to millennial cycles, estimated at about 1.5 to 6 kyr. Nevertheless, the most reliable cyclicity information (periodic or nearly periodic variations) comes from the spectral analysis of physical ($\overline{SS}$) and chemical (Zr/Al ratio) bottom current proxies (Fig. 8).

Spectral analysis of both bottom current proxies reveals statistically significant oscillations at sub-orbital and millennial scales. Cycles centered at 1900 yr, 2300 yr, 4000 yr, and 6200 yr are identified (Fig. 8). These cycles would potentially be linked to both oceanic and solar forcing mechanisms (internal and external forcing), which may have contributed to increased deep-water formation in the NW Mediterranean and resulted in variations of WMDW flow. The millennial periodicities closely coincide with paleoclimatic records from Northern Hemisphere high latitudes (*e.g.,* cycles of 1.3, 1.5, 1.8, 2.3, 3.8 and 6.3; Bond et al., 1993, 1997; Mayewski et al., 1997; Oppo et al., 1998; Goslin et al., 2018). Such correlation suggests links between the Western Mediterranean Sea and higher latitude climatic systems, or at least hints at a similar forcing mechanism. These findings support a close relationship between the deep-water variability and rapid climatic oscillations in the Mediterranean region. The nearly periodic 1500 yr variability identified in the Western Mediterranean (Moreno et al., 2004; Rodrigo-Gámiz et al., 2014) and North Atlantic (Mayewski et al., 1997) was not detected in our Alboran records, however.

The 1900 yr cycle is present in the spectral analysis of Zr/Al ratio (peak at 1912 yr) with CL of 93% (Fig. 8B). This cycle might be equivalent to the 1800 yr cycle identified in the spectral analysis of time series of hematite-stained grains used as paleoclimate proxy in the North Atlantic (Bond et al., 1997), a 1000–2000 yr cycle in the percentage of these lithic grains spanning the entire interval from the Holocene through half of sub-stage 5a (MIS 5). Alternatively, the cycle of 1900 yr seen in spectral signature of Zr/Al ratio also closely matches the 2000 yr cycle recently described along the Iberian margin over the last 420 kyr using alkenone as the paleotemperature proxy (Rojo-Garibaldi et al., 2020).

The 2300 yr cycle is well represented in the spectral analysis of both bottom current proxies (peak at 2292 yr for $\overline{SS}$ with CL 97%, peak at 2312 yr for Zr/Al ratio with CL 99%; Fig. 8). This cycle resembles the one described by Bray (1968), who identified cycles of solar activity (external forcing) with a frequency of 2500 yr by means of a geophysical and glaciological approach. The solar imprint of the 2500 yr cycle is evident in both hemispheres during the Holocene (Debret et al., 2007), demonstrating that atmospheric circulation records may contain embedded evidence of solar-climate relationships (Mayewski et al., 2004; McCracken et al., 2013). The findings from this core were tied to well-known rapid climatic oscillations, ranging from 1000 to 3000 yr, described in glacial records of Greenland ice cores (Grootes et al., 1993) and related to Bond cycles. Consequently, the 2300 yr cycle may represent Bond cycles as well.

The 4000 yr cycle is present in the spectral signature of the Zr/Al ratio (peak at 3975 yr; Fig. 8B) with high CL (up to 99%). Recently, a climatic time series recording up to 420 kyr found the same 4000 yr cycle for the Iberian margin region (Rojo-Garibaldi et al., 2020). According to their results, this cycle affected not only MIS1 and MIS2, but stretched all the way down to MIS 11. It comes to close an ice-rafted debris event centered at 4200 yr (Holocene in the Atlantic) that provided evidence of a close link between the shifts in Holocene climate and atmospheric circulation above Greenland (Bond et al., 1997). This cycle might further provide evidence of coupled ocean-atmosphere modes of variability on a millennial scale in the Alboran Sea.

The 6200 yr cycle is recorded in the spectral signature of the Zr/Al ratio (peak at 6200 yr; Fig. 8B) with very high CL (up to 99%). It nearly matches the 6100 yr cycle described by Bond et al. (1993), which mirrors the timing of ice-rafted marine debris events ascribed to ice sheet dynamics, revealing a strong association with the timing of HSs. This cycle is ascribed primarily to insolation-induced ice sheet volume changes in agreement with the roughly 6100 yr cyclic behavior predicted by simple ice sheet oscillation models (MacAyeal, 1993). Mayewski et al. (1997) point out that the cycle of 6100 yr cooling appeared to not be solely related to ice sheet dynamics, but also to other mechanisms allowing suborbital-scale changes in insolation to be translated through the ocean-atmosphere cryosphere system into climate changes. Such an interpretation leads us to consider that the D—O cycles and HS events that are repeated every 5000–10000 yr were the most significant ones recorded in the SW Mediterranean. The presence of this cycle in the Alboran record suggests that changes in environmental conditions were more severe during these events, particularly with regard to aridity in the nearby borderland, as was mentioned for the HSs deposited from 28 to 50 kyr (Moreno et al., 2005). More detailed

climate modelling would be needed to fully understand the relationship between the cycles behind internal and external forcings and their consequences as bottom current variations in the Western Mediterranean.

The stratigraphic records of cores C8 and M8 provide additional evidence of the strong links between contourites and climate in the Alboran basin. Detailed examination of the silty layer distribution in conjunction with the signature of planktonic oxygen isotopes serve to demonstrate climatic control upon the contourite deposition (Fig. 5). The silty layers —represented by sandy silt (EM1) and clayey silt (EM2)— and the peaks of $\overline{SS}$ present in both cores correlate most of them with cooling episodes recorded in the planktonic oxygen isotope record ($\delta\ ^{18}O$) of core C8, suggesting climatic control of the silty layers and bottom current enhancement (Fig. 5). The coldest events (HS2, HS1, and YD) recognized in the record, with surface temperature drops of 4 °C (Cacho et al., 1999; Pérez-Folgado et al., 2003; Martrat et al., 2004), are accompanied by increases in grain-size (Fig. 3). In addition, ample changes in bottom current strength and arid conditions are revealed by the correlation between grain-size and sediment compositional changes (Fig. 4). The highest peaks of median grain-size and maximum scores of EM1 (sandy silt) and EM2 (clayey silt) are followed by high peaks of a chemical bottom current proxy (Zr/Al ratio) and an arid chemical proxy (Si/(Si + Al) ratio). This indicates that the silty sediments (coarse and fine silt) were deposited under enhanced bottom currents during arid conditions, implying stronger winds and atmospheric circulation changes. Such a scenario is consistent with previous evidence that cold stadials are associated with enhanced WMDW formation, due to more arid conditions and stronger northwesterlies over the Western Mediterranean (Cacho et al., 2000; Moreno et al., 2005). Additionally, low values of Zr/Al and Si/(Si + Al) ratios correlate with maximum scores of EM3 (silty clay), marking more humid conditions during the deposition of these sediments (Fig. 4A).

5.4. Paleoceanographic implications for the Western Mediterranean

Given the strategic locations of the Alboran contourite drifts, reconstructions of past WMDW flow (inferred by $\overline{SS}$ measurements) can be derived from its upstream to downstream location, providing a comprehensive basin-scale view (Fig. 1B). By adding the $\overline{SS}$ record of core MD99–2343, retrieved from an elongated separated contourite drift in the NW Mediterranean (Fig. 1A, Frigola et al., 2008), the paleoceanographic reconstruction of the WMDW can be expanded to the entire Western Mediterranean (Fig. 10). The suitability of core MD99–2343 is explained in Section 3 of Supplementary data. These three cores provide a high resolution time window, allowing for the reconstruction of paleoceanographic and paleoclimatic oscillations since the LGM in the Western Mediterranean. Some of the major paleoclimatic changes closely correlated with climatic oscillations recorded in Greenland ice cores support the connection between high- and mid-latitude climates (*i.e.,* Moreno et al., 2005; Jiménez-Espejo et al., 2007; Frigola et al., 2008).

5.4.1. Millennial synchronous events of WMDW flow

Four main synchronous phases (labelled I to IV, from older to younger) define the WMDW flow for the last 25 cal. kyr BP (Fig. 10A) and reflect concurrent paleoceanographic and climate changes. Phases I, II and III occur between the end of HS2 and the onset of the Holocene and display a similar trend: current acceleration, maximum flow velocity is reached during a fast current event (FCE), which is followed by current deceleration (Fig. 10A). Phase IV occurs between the onset of the Holocene and the present, and shows a complex pattern characterized by current acceleration followed by a period of comparatively steady velocity and, eventually, current deceleration (Fig. 10A). The four synchronous phases identified by the $\overline{SS}$ records imply that over time the position/depth of the WMDW flow was relatively stable or, at least its high-velocity axis did not shift substantially across the coring sites during the last 25 cal. kyr BP. Despite the overall synchronous phases of the WMDW flow, in detail two non-synchronous events stand out (Section 5.4.2).

Phase I (~24.2–18 cal. kyr BP) corresponds to most of the LGM (the interval between 23 and 19 cal. kyr BP according to Mix et al., 2001; Fig. 10A). It starts with a gradual enhancement of WMDW flow velocities and ends with FCE-I around 20 cal. kyr BP, reaching velocities from ~9 to ~19 cm s^{-1} ("Ia" in Table 2). The change in velocity is also reflected in the Zr/Al ratio, which attains a relative maximum (Fig. 3). FCE-I roughly coincides with a cold interval (~20.5 cal. kyr BP) already defined in the Alboran basin (Cacho et al., 2006). This FCE involves clayey silt/sandy silt deposits in cores M8/C8, respectively, together with a peak in the Zr/Al and Si/(Si + Al) ratios (Figs. 3, 4). All of these findings point to arid conditions during the event. Toward the end of phase I (~18 cal. kyr BP), a weakening of WMDW flow is observed, reaching paleo-velocities from 5 to 14 cm s^{-1} ("Id" in Table 2), in conjunction with wetter conditions and increased river discharge, as indicated by the decrease in the arid proxy (Si/(Si + Al) ratio). Previous studies have also referred to this change (Combourieu-Nebout et al., 2009; Ausín et al., 2015).

Phase II (~18–15 cal. kyr BP) ranges from the end of the LGM to HS1 (Fig. 10A). Similar to phase I, it starts a current acceleration, ending with FCE-II at ~16 cal. kyr BP (reaching paleo-velocities from ~9 cm s^{-1} to ~17 cm s^{-1}, "IIa" in Table 2). FCE-II coincides with the second part of HS1. This second FCE is also evidenced by coarse/fine silt in cores C8/M8, respectively, and it occurred during colder (SST down to 2 °C, Ausín et al., 2015) and arid conditions, the latter revealed by the increase of the Si/(Si + Al) ratio (Figs. 3, 4). A slight weakening of the WMDW flow (between ~6 and ~12 cm s^{-1}, "IId" in Table 2) followed this FCE. Warmer conditions during the weakening period are marked by oxygen isotope depletion in cores C8 and M8 (Fig. 5) and are described by Ausín et al. (2015). Nevertheless, detailed examination of $\overline{SS}$ during HS1 reveals a tri-phase pattern (increase-decrease-increase, Fig. 10A) linked to the three stages (early, middle, and late) previously documented in marine sequences during HS1. High sedimentation rates in the Western Mediterranean are reported during that period (Frigola et al., 2007; Rodrigo-Gámiz et al., 2014; Bazzicalupo et al., 2020). It has been suggested that HSs have a complex bottom current evolution, with stronger flow and high ventilation during the early and late stages, and a weakening in the middle stage due to surface freshening tied to the entry of (colder) polar surface water through the Strait of Gibraltar (Sierro et al., 2005; Cacho et al., 2006).

Phase III (15–10.3 cal. kyr BP) comprises the B-A, YD and onset of the Holocene (Fig. 10A). It starts with an enhancement of the WMDW flow that ends with a marked FCE-III at around 12.8 cal. kyr BP reaching paleo-velocities from ~11 to ~23 cm s^{-1} ("IIIa" in Table 2). This third FCE is associated with the YD, which developed a particular signal in the Mediterranean basin distinguishing it from other northern hemispheric regions where the internal variability has not been documented (McCave et al., 1995). This FCE involves clayey silt/sandy silt, respectively in cores M8/C8, and coincides with a clear maximum peak in the Zr/Al ratio (Figs. 3, 4). These enhanced $\overline{SS}$ values during the YD are also consistent with the coarser contouritic deposit detected in the Gulf of Cadiz, suggesting that the detected enhanced energy was also transferred into the Mediterranean Outflow Waters (Toucanne et al., 2007; Lebreiro et al., 2018). FCE-III occurred during an arid —note the most pronounced increase of the arid proxy (Si/(Si + Al) ratio; Figs. 3, 4A) — and cold period, indicated by oxygen isotope highs in cores C8 and M8 (Fig. 2). In detail, the $\overline{SS}$ record for YD reflects an increase from 13 to 12.5 cal. kyr BP and a decrease from 12.5 to 11.7 cal. kyr BP (Fig. 10A), corresponding to two stages: the first, cold/arid; the second, warm/wet (Cacho et al., 2001). As such, the $\overline{SS}$ record indicates the previously identified internal variability during the YD in the Mediterranean Sea (Frigola et al., 2007; Rodrigo-Gámiz et al., 2011; Ausín et al., 2015),

with an abrupt drop in sea surface temperatures (up to 3 °C) and a rapid warming (up to 6 °C; Ausín et al., 2015). Following FCE-III, a deceleration of the WMDW takes place (velocities from ~4 to ~9 cm s^{-1}, "IIId" in Table 2). The important decrease in $\overline{SS}$, Zr/Al and Si/(Si + Al) ratios, all reaching minimum values between 10 and 11.3 cal. kyr BP (early Holocene), is consistent with the most pronounced weakening of the Mediterranean thermohaline circulation at that time (Frigola et al., 2008). This weakening is a well-marked period in the Western Mediterranean, characterized by the end of deposition of an organic rich layer (Cacho et al., 2001; Jiménez-Espejo et al., 2008). Warmer conditions, as seen in the surface temperature by Ausín et al. (2015), and more humid ones, deduced from the substantial decrease of the arid proxy Si/(Si + Al) ratio prevailed (Fig. 4A). The very weak WMDW currents in the NW Mediterranean during this period (Fig. 10A) could reflect enhanced vertical stratification promoted by freshwater input from the Rhone River, along with increased precipitation during the summer insolation maximum (Frigola et al., 2007).

Phase IV (~10.3 cal. kyr BP to present) covers the onset of the Holocene up to late Holocene (Fig. 10A) and is similar to the stage defined by Frigola et al. (2008) with regard to the Menorca Drift. It begins with an enhancement of WMDW that ends with the FCE-IV, reaching paleo-velocities from ~6 to ~17 cm s^{-1} ("IVa" in Table 2). These findings are linked to an abrupt transition from warmer to cold conditions. The general trend in the mid-Holocene is represented by maximum paleo-velocities (*i.e.*, ~5.4 to 18 cm s^{-1}) similar to those of FCE-IV (Fig. 10A), and ends with a general weakening to paleo-velocities of ~4 to ~9 cm s^{-1} in the late Holocene ("IVd" in Table 2). The Holocene climate variability is of a lower magnitude (Debret et al., 2009), most likely reflected in the stabilizing WMDW trend during phase IV deduced from the $\overline{SS}$ records (Fig. 10A). Since climate change and sea-level rise go hand in hand during the Holocene in the Alboran (Cacho et al., 2001), sea-level changes also influenced the Western Mediterranean thermohaline circulation and build-up of the studied contourite drifts. Moreover, the WMDW changes during this phase —enhancement, stabilization, then weakening— largely fit with three surface hydrographic and climate periods (early, middle and late Holocene) documented recently by Bazzicalupo et al. (2020).

5.4.2. Non-synchronous events of the WMDW flow

Two non-synchronous events are identified for the last 25 cal. kyr BP (Fig. 10C). One occurred during the end of HS2 (23.5–22.5 cal. kyr BP), when an increase in $\overline{SS}$ is observed in cores C8 and MD99–2343 (the deepest cores), while a decreasing pattern is registered in the shallower core M8. This pattern should point to a deepening of the vertical position of WMDW, leaving core M8 no longer (or only partly) affected by this water mass. The other non-synchronous phase took place during the early Holocene (11–10 cal. kyr BP) and is characterized by an increase in $\overline{SS}$ in core C8 and a decreasing pattern in cores M8 and MD99–2343. The presence of WMDW at the location of core C8 might explain the stronger $\overline{SS}$ values, while the Menorca Drift was not influenced, hence low $\overline{SS}$ values (Fig. 10A). The fact that core M8 (unlike core C8) did not record a similar current invigoration may indicate a different pathway for this water mass (possibly along the Spanish margin, as modern intermediate waters), or a lesser contribution of WMDW into the Mediterranean outflow. In fact, a recent study based on the analysis of benthic foraminifer assemblages from Western Mediterranean cores at different depths also infers deepening WMDW at that time related to the appearance of a distinctive intermediate water mass (Pérez-Asensio et al., 2020). Considering all the above, variations in the WMDW core location —both laterally and vertically— rather than a variation in WMDW characteristics *per se*, would explain the observed differences in $\overline{SS}$. We hypothesize two possible situations: i) local hydrological changes in the WMDW core, close to the Strait of Gibraltar, and ii) a local change in the WMDW characteristics due to mixing. The local hydrological changes could result from changes in the Western Alboran Gyre, favoring enhanced ventilation of WMDW that (at present) can reach waters from depths as great as 700 m (Stommel et al., 1973; Naranjo et al., 2012). Enhancement in the gyre dynamics would favor a local increase in bottom current velocity, in turn reflected by an increase in the $\overline{SS}$ pattern in core C8. The local change in the WMDW characteristics due to mixing processes should be reflected by local SST reconstructions. This hypothesis could be supported by a short cooling in the alkenone-SST record from core C8 (Ausín et al., 2015), although a strongest cooling signal is found in the Mg/Ca-SST record of neighboring core -ALB2 studied by Català et al. (2019). Recent analyses of the time window of Organic Rich Layer formation (ORL, 14.5 to 8.2 cal. kyr BP) emphasizes the role of shoaling in the interface between intermediate and deep-waters during the deglaciation period (Rogerson et al., 2008; Pérez-Asensio et al., 2020). Consequently, the direct vertical mixing between the Atlantic Waters and the Mediterranean Waters (including the WMDW) would also be uplifted, increasing the supply of nutrients to the surface. This interpretation is supported by the increase in productivity during the time interval of ORL deposition revealed by recent works (Jiménez-Espejo et al., 2008; Ausín et al., 2015).

6. Conclusions

The present study is based on sedimentological and geochemical data as well as derived statistical analyses (*e.g.,* grain-size end-member modelling and spectral analyses). Regarding the interaction between bottom currents and contourite sediment distribution, this work highlights the following points.

1. The sedimentological and geochemical results emphasize the significant impact of bottom current activity on the Alboran contourite drifts. The contourite drifts comprise three contourite sequence types: sequences Sa (mud, fine silt, and mud), Sb (coarse silt, fine silt, and mud), and Sc (sand), which are respectively equivalent to the generic divisions C4–5 (or C1–2), C2–3-4, and C3 of the contourite model. Cyclic contourite variations at sub-orbital and millennial scales are revealed by spectral analysis of $\overline{SS}$ and the Zr/Al ratio, proxies used as tracers for deep-water circulation. These variations are dominated by 1900 yr, 2300 yr, 4000 yr, and 6200 yr cycles, related to atmospheric climate variability, in turn linked to variations in solar activity.
2. The $\overline{SS}$ records of the SW Mediterranean cores provide a continuous high-resolution record of WMDW flow velocity variability at a regional scale. In this framework, two regimes in terms of energy of WMDW flow controlled the deposition of these three contourite sequences. Weak to moderate velocity models were estimated between 4 and 23 cm s^{-1} (represented by Sa and Sb), and a high velocity model reached up to ~36 cm s^{-1} (represented by Sc). The WMDW flow paleo-velocity moreover varies at a local scale, linked to singular oceanographic and topographic conditions in the proximity of the Strait of Gibraltar. Estimated paleo-velocities in the elongated contourite drift may be enhanced and conditioned by oceanographic and physiographic conditions. Therefore, the plastered contourite drift appears to better represent WMDW flow paleo-velocities, as compared to the elongated contourite separated drift.
3. The detailed comparison of $\delta^{18}O$ and $\overline{SS}$ records in the SW Mediterranean, complemented with some of the already existing $\overline{SS}$ records in the NW Mediterranean, provides for a high-resolution reconstruction of WMDW dynamics over the last 25 cal. kyr BP. The most noteworthy finding is the similar trend of WMDW flow paleo-velocity at the millennial scale, allowing us to define for the first time four synchronous phases related to climatic periods —the LGM, HS1, YD and Holocene— and with repercussions for the ventilation rates of deep-ocean circulation. Another important result is the presence of two previously undocumented non-synchronous events of WMDW flow, apparently related to local hydrological changes

near the Strait of Gibraltar, and/or a local change in the WMDW characteristics due to mixing processes.

4. This work sheds new light on WMDW dynamics, estimating the paleo-velocity variability during the last 25 cal. kyr BP, while also affording a framework for the interpretation of time records of $\overline{SS}$ in the Western Mediterranean region. Finally, the strategy followed in this research, coring several well-chosen sites along the outflow path of WMDW, with the combined use of qualitative and quantitative tools, is undoubtedly the most desirable approach to understand paleochanges in the WMDW flow velocity and their relationship with climatic changes.

Supplementary data to this article can be found online at https://doi.org/10.1016/j.margeo.2021.106488.

Declaration of Competing Interest

None.

Acknowledgements

We would like to acknowledge the financial support provided by the "Ministerio de Ciencia, Innovación y Universidades" of Spain in the framework of FAUCES project (CTM2015-65461-C2-2-R), CONTOURIBER project (CTM2008-06399-C04/MAR) and MONTERA (CTM2009-14157-C02). Research by RT was funded by Project PID2019-104625RB-100 (Secretaría de Estado de I + D + I, Spain), B-RNM-072-UGR18 (FEDER Andalucía), and P18-RT-4074 (Junta de Andalucía). This work also acknowledges the 'Severo Ochoa Centre of Excellence' accreditation (CEX2019-000928-S).

References

Alonso, B., Ercilla, G., Casas, D., Stow, D.A.V., Rodríguez-Tovar, F.J., Dorador, J., Hernández-Molina, F.J., 2016. Contourite vs gravity-flow deposits of the Pleistocene Faro Drift (Gulf of Cadiz): sedimentological and mineralogical approaches. Mar. Geol. 377, 77–94.

Andrews, J.T., Hardadottir, J., Stoner, J.S., Man, M.E., Kristjansdottir, G.B., Koc, N., 2003. Decadal to millennial-scale periodicities in North Iceland shelf sediments over the last 12000 cal. yr: long-term North Atlantic oceanographic variability and solar forcing. Earth Planet. Sc. Lett. 210, 453–465.

Ausín, B., Flores, J.A., Sierro, F.J., Barcena, M.A., Hernández-Almeida, I., Francés, G., Gutiérrez-Arnilla, E., Martrat, B., Grimalt, J., Cacho, I., 2015. Coccolithophore productivity and surface water dynamics in the Alboran Sea during the last 25 kyr. Palaeogeo. Palaeoclima. Palaeocol. 418, 126–140.

Bahr, A., Jiménez-Espejo, F.J., Kolasinac, N., Grunert, P., Hernández-Molina, F.J., Röhl, U., Voelker, A.H.L., Escutia, C., Dorrik, A.V., Stow, D.A.V., Hodell, D., Alvarez-Zarikian, C., 2014. Deciphering bottom current velocity and paleoclimate signals from contourite deposits in the Gulf of Cadiz during the last 140 kyr: an inorganic geochemical approach. Geochem. Geophys. Geosyst. 13, 3145–3160.

Bazzicalupo, P., Maiorano, P., Girone, A., Marino, M., Combourieu-Nebout, N., Pelosi, N., Salgueiro, E., Incarbona, A., 2020. Holocene climate variability of the Western Mediterranean: surface water dynamics inferred from calcareous plankton assemblages. The Holocene 1–18. https://doi.org/10.1177/0959683619895580.

Bender, V.B., Hanebuth, T.J.J., Mena, A., Baumann, K.H., Francés, G., Dobeneck, T., 2012. Control of sediment supply, palaeogeography and morphology on late Quaternary sediment dynamic at the Galicia continental slope. Geo-Mar. Lett. 32, 313–335.

Béthoux, J.P., 1979. Budgets of the Mediterranean Sea: their dependence on the local climate and on the characteristics of the Atlantic Water. Oceanol. Acta 7 (3), 289–2996.

Bianchi, G.G., McCave, N., 1999. Holocene periodicity in North Atlantic climate and deep-ocean flow south of Iceland. Nature 397 (6719), 515–517.

Bianchi, G.G., Vautravers, M., Shackleton, N.J., 2001. Deep flow variability under apparently stable North Atlantic Deep Water production during the last interglacial of the subtropical NW Atlantic. Paleoceanogr 16 (3), 306–316.

Blott, S.J., Pye, Q., 2001. Gradistat: a grain size distribution and statistics package for the analysis of unconsolidated sediments. Earth Surf. Proc. Landforms 26, 1237–1248.

Bond, G., Broecker, W., Johsen, S., McManus, J., Labeyrie, L., Jouzel, J., Bonani, G., 1993. Correlations between climate records from North Atlantic sediments and Greenland ice. Nature 365, 143–147.

Bond, G., Showers, W., Cheseby, M., Lotti, R., Almasi, P., deMenocal, P., Priore, P., Cullen, H., Hajdas, I., Bonani, G., 1997. A pervasive millennial-scale cycle in North Atlantic Holocene and glacial climates. Science 278, 1257–1266.

Brackenridge, R., Stow, D.A.V., Hernández-Molina, F.J., Jones, C., Mena, A., Alejo, I., Ducassou, E., Llave, E., Ercilla, G., Nombela, M.A., Pérez-Arlucea, M., Francés, G., 2018. Textural characteristics and facies of sand-rich contourite depositional systems. Sedimentol. https://doi.org/10.1111/sed.12463.

Bray, J.R., 1968. Glaciation and solar activity since the fifth century BC and the solar cycle. Nature 220, 672–674.

Broecker, W.S., 1991. The great ocean conveyor. Oceanogr 4 (2), 79–89. https://doi.org/10.5670/oceanog.1991.07.

Bryden, H.L., Stommel, H.M., 1982. Origin of the Mediterranean Outflow. J. Mar. Res. 40 (suppl), 55–71.

Cacho, I., Grimalt, J.O., Pelejero, C., Canals, M., Sierro, F.J., Flores, J.A., Shackleton, N. J., 1999. Dansgaard-Oeschger and Heinrich event imprints in Alboran Sea paleotemperatures. Paleoceanogr 14 (6), 698–705.

Cacho, I., Grimalt, J.O., Sierro, F.J., Shackleton, N.J., Canals, M., 2000. Evidence for enhanced Mediterranean thermohaline circulation during rapid climate coolings. Earth Planet. Sci. Lett. 183, 417–429.

Cacho, I., Grimalt, M., Canals, M., Sbaffi, J., Shackleton, J., Schonfeld, J., Zahn, R., 2001. Variability of the Western Mediterranean Sea-surface temperature during the last 25000 years and its connection with the Northern-Hemisphere climatic changes. Paleoceanogra 16, 40–52.

Cacho, I., Shackleton, N., Elderfield, H., Sierro, F.J., Grimalt, J., 2006. Glacial rapid variability in deep-water temperature and $\delta^{18}O$ from the Western Mediterranean Sea. Quaternary Sci. Rev. 25 (23–24), 3294–3311.

Català, A., Cacho, I., Frigola, J., Pena, L.D., Lirer, F., 2019. Holocene hydrography evolution in the Alboran Sea: a multi-record and multi-proxy comparison. Clim. Past 15, 927–942.

Colmenero-Hidalgo, E., Flores, J.A., Sierro, F.J., Barcena, M.A., Lowemark, L., Schönfeld, J., Grimalt, J., 2004. Ocean surface water response to short-term climate changes revealed by coccolithophores from the Gulf of Cadiz (NE Atlantic) and Alboran Sea (W Mediterranean). Palaeogeogr. Palaeoclimatol. Palaeoecol. 205, 317–336.

Combourieu-Nebout, N., Peyron, O., Dormoy, I., Desprat, S., Beaudouin, C., Kotthoff, U., Marret, F., 2009. Rapid climatic variability in the West Mediterranean during the last 25000 years from high-resolution pollen data. Clim. Past 5, 503–521.

Coplen, T.B., 1996. New guidelines for reporting stable hydrogen, carbon, and oxygen isotope- ratio data. Geochim. Cosmochim. Acta 60, 3359–3360. https://doi.org/10.1016/0016-7037(96)00263-3.

Cremer, M., Faugères, J.C., Grousset, F., Gonthier, E., 1993. Late Quaternary sediment flux on sedimentary drift in the Northeast Atlantic. Sediment. Geol. 82, 89–111.

Debret, M., Bout-Roumazeilles, V., Grousset, F., Desmet, M., McManu, J.F., Massei, N., Sebag, D., Petit, J.R., Copard, Y., Trentesaux, A., 2007. The origin of the 1500-year climate cycles in Holocene North-Atlantic records. Clim. Past 3, 569–575.

Debret, M., Sebag, D., Crosta, X., Massei, M., Petit, J.R., Chapron, E., Bout-Roumazeilles, V., 2009. Evidence from wavelet analysis for a mid-Holocene transition in global climate forcing. Quat. Sci. Rev. 28 (25–26), 2675–2688.

Dietze, E., Maussion, F., Ahlborn, M., Diekmann, B., Hartmann, K., Henkel, K., Kasper, T., Lockot, G., Opitz, S., Haberzettl, T., 2014. Sediment transport processes across the Tibetan plateau inferred from robust grainsize end members in lake sediments. Clim. Past 10, 91–106.

Dorador, J., Rodríguez-Tovar, F.J., 2018. High-resolution image treatment in ichnological core analysis: initial steps, advances and prospects. Earth Sci. Rev. 177, 226–237.

Dorador, J., Rodríguez-Tovar, F.J., IODP Expedition 339 Scientists, 2014a. Digital image treatment applied to ichnological analysis of marine core sediments. Facies 60, 39–44.

Dorador, J., Rodríguez-Tovar, F.J., IODP Expedition 339 Scientists, 2014b. Quantitative estimation of bioturbation based on digital image analysis. Mar. Geol. 349, 55–60.

Dorador, J., Rodríguez-Tova, F.J., Mena, A., Francés, G., 2019. Lateral variability of ichnological content in muddy contourites: weak bottom currents affecting organisms' behavior. Sci. Rep. Nat. Res. 9, 17713. https://doi.org/10.1038/s41598-019-54246-3.

Dorador, J., Rodríguez-Tovar, F.J., Titschack, J., 2020. Exploring computed tomography in ichnological analysis of cores from modern marine sediments. Sci. Report. 10, 201. https://doi.org/10.1038/s41598-019-57028-z.

Ercilla, G., Baraza, J., Alonso, B., Estrada, F., Casas, D., Farran, M., 2002. The Ceuta Drift, Alboran Sea, Southwestern Mediterranean. Geol. Soc. Lond. Mem. 22 (1), 155–170.

Ercilla, G., Juan, C., Hernández-Molina, F.J., Bruno, M., Estrada, F., Alonso, B., Casas, D., Farran, M., Llave, E., García, M., Vázquez, J.T., d'Acremont, E., Gorini, C., Palomino, D., Valencia, J., El Moumni, B., Ammar, B., 2016. Significance of bottom currents in deep-sea morphodynamics: an example from the Alboran Sea. Mar. Geol. 378, 157–170.

Ercilla, G., Juan, C., Periáñez, R., Alonso, B., Abril, J.M., Estrada, F., Casas, D., Vázquez, J.T., D'acremont, E., Gorini, C., El Moumni, B., do Couto, D., Valencia, J., 2019. Influence of alongslope processes on modern turbidite systems and canyons in the Alboran Sea (Southwestern Mediterranean). Deep-Sea Res. Part I Oceanogr. 144, 1–16.

Evans, H.K., Hall, I.R., 2008. Deepwater circulation on Blake Outer Ridge (Western North Atlantic) during the Holocene, Younger Dryas, and Last Glacial Maximum. Geochem. Geophys. Geosyst. 9 (3), Q03023 https://doi.org/10.1029/2007GC001771.

Fabres, J., Calafat, A., Sanchez-Vidal, A., Canals, M., Heussner, S., 2002. Composition and spatio-temporal variability of particle fluxes in the Western Alboran Gyre, Mediterranean Sea. J. Mar. Syst. 33-34, 431–456. https://doi.org/10.1016/S0924-7963(02)00070-2.

Faugères, J.C., Mulder, T., 2011. Contour Currents and Contourite Drifts, in: Hüneke, H.

Faugères, J.C., Stow, D.A.V., 1993. Bottom-current-controlled sedimentation: a synthesis of the contourite problem. Sediment. Geol. 82, 287–297.

Faugères, J.C., Gonthier, E., Stow, D.A.V., 1984. Contourite drift molded by deep Mediterranean outflow. Geology 12, 296–300.

Fink, H.G., Wienberg, C., De Pol-Holz, R., Wintersteller, P., Hebbeln, D., 2013. Cold-water coral growth in the Alboran Sea related to high productivity during the Late Pleistocene. Mar. Geol. 339, 71–82.
Frigola, J., Moreno, A., Cacho, I., Canals, M., Sierro, F.J., Flores, J.A., Grimalt, J.O., Hodell, D.A., Curtis, J.H., 2007. Holocene climate variability in the Western Mediterranean region from a deep-water sediment record. Paleoceanogr. Paleoclima. 22 (2), 1–16.
Frigola, J., Moreno, A., Cacho, I., Canals, M., Sierro, F.J., Flores, J.A., Grimalt, J.O., 2008. Evidence of abrupt changes in Western Mediterranean Deep Water circulation during the last 50 kyr: a high-resolution marine record from the Balearic Sea. Quat. Int. 181 (1), 88–10.
Gascard, J.C., Richez, C., 1985. Water masses and circulation in the Western Alboran Sea and in the Strait of Gibraltar. Prog. Ocean. 15 (3), 157–216.
Goslin, J., Fruergaard, M., Sander, L., Galka, M., Menviel, L., Monkenbuch, J., Thiabault, N., Clemmensen, L., 2018. Holocene centennial to millennial shifts in North-Atlantic storminess and ocean dynamics. Sci. Report. 8 (12778) https://doi.org/10.1038/s41598-018-299949-8.
Grootes, P., Stuiver, M., White, J.W.C., Johnsen, J., Jouzel, J., 1993. Comparison of oxygen isotope records from the GISP2 and GRIP Greenland ice cores. Nature 366, 552–554.
Hamann, Y., Ehrmann, W., Schmiedl, G., Krüger, S., Stuut, J.B., Kuhnt, T., 2008. Sedimentation processes in the Eastern Mediterranean Sea during the late glacial and Holocene revealed by end-member modelling of the terrigenous fraction in marine sediments. Mar. Geol. 248, 97–114.
Hoogakker, B.A.A., Chapman, M.R., McCavw, I.N., 2011. Dynamics of North Atlantic Deep Water masses during the Holocene. Paleoceanogr 26 (4), PA4214. https://doi.org/10.1029/2011PA002155.
Howe, J.A., Stoker, M.S., Stow, D.A.V., 1994. Late Cenozoic sediment drift complex, Northeast Rockall Trough, North Atlantic. Paleoceanogr 9 (6), 989–999.
Jiménez-Espejo, F.J., Martínez-Ruiz, F., Sakamoto, T., Iijima, K., Gállego-Torres, D., Harada, N., 2007. Paleoenvironmental changes in the Western Mediterranean since the last glacial maximum: high-resolution multiproxy a record from the Algero-Balearic basin. Palaeogeogr. Palaeoclimatol. Palaeoecol. 246, 292–306.
Jiménez-Espejo, F.J., Martínez-Ruiz, F., Rogerson, M., González-Donoso, J.M., Romero, O.E., Linares, D., Sakamoto, T., Gallego-Torres, D., Rueda-Ruiz, J.L., Ortega-Huertas, M., Pérez-Claros, J.A., 2008. Detrital input, productivity fluctuations, and water mass circulation in the westernmost Mediterranean Sea since the Last Glacial Maximum. Geochem. Geophys. Geosyst. 9 (11) https://doi.org/10.1029/2008GC002096.
Jiménez-Moreno, G., Aziz, H.A., Rodríguez-Tovar, F.J., Pardo-Igúzquiza, E., Su, J.P., 2007. Palynological evidence for astronomical forcing in Early Miocene lacustrine deposits from Rubielos de Mora Basin (NE Spain). Palaeogeogr. Palaeoclimatol. Palaeoecol. 252, 601–616.
Juan, G., Ercilla, G., Hernández-Molina, F.J., Estrada, F., Alonso, B., Casas, D., García, M., Farran, M., Llave, E., Palomino, D., Vázquez, J.T., Medialdea, T., Gorini, C., d'Acremont, E., El Moumni, B., Ammar, A., 2016. Seismic evidence of current-controlled sedimentation in the Alboran Sea during the Pliocene and Quaternary: palaeoceanographic implications. Mar. Geol. 378, 292–311.
Juan, C., Ercilla, G., Estrada, F., Alonso, B., Casas, D., Vázquez, J.T., d'Acremont, E., Medialdea, T., Hernández-Molina, F.J., Gorini, C., Moumni, B., Valencia, J., 2020. Multiple factors controlling the deep marine sedimentation of the Alboran Sea (SW Mediterranean) after the Zanclean Atlantic Mega-flood. Mar. Geol. 423, 106–138.
Knaust, D., 2017. Atlas of trace fossils in well core. In: Appearance, Taxonomy and Interpretation. Springer.
Knutz, P.C., 2008. Paleoceanographic significance of contourite drifts. In: Rebesco, M., Camerlenghi, A. (Eds.), Developments in Sedimentology. Elsevier, pp. 511–535.
Kuhlbrodt, T., Griesel, A., Montoya, M., Levermann, A., Hofmann, M., Rahmstorf, S., 2007. On the driving processes of the Atlantic meridional overturning circulation. Rev. Geophys. 45 (2), 2004RG000166.
Kuhn, G., Diekmann, B., 2002. Data report: Bulk sediment composition, grain size, clay and silt mineralogy of Pleistocene sediments from ODP Leg 177 Sites 1089 and 1090. In: Gersonde, R., Hodell, D.A., Blum, P. (Eds.), Proceedings. ODP, Sci. Results, 177, pp. 1–10.
Lamy, F., Arz, H.W., Kilian, R., Lange, C., Lembke-Jene, L., Wengler, M., Kaiser, J., Baeza-Urrea, O., Hall, I.R., Harada, N., Tiedemann, R.F., 2015. Glacial reduction and millennial-scale variations in Drake Passage through flow. PNAS 112 (44), 13496–13501.
Lebreiro, S.M., Antón, L., Reguera, M.I., Marzocchi, A., 2018. Paleoceanographic and climatic implications of a new Mediterranean Outflow branch in the southern Gulf of Cadiz. Quat. Sci. Rev. 197, 92–111.
Liquete, C., Arnau, P., Canals, M., Colas, S., 2005. Mediterranean river systems of Andalusia, southern Spain, and associated deltas: a source to sink approach. Mar. Geol. 222-223 (15), 471–495.
Lobo, F.J., Ercilla, G., Fernández-Salas, L.M., Gámez, D., 2014. The Iberian Mediterranean shelves. Geol. Soc. Lond. Mem. 41 (1), 147–170.
López-González, N., Alonso, B., Juan, C., Ercilla, G., Graziella, G., Cacho, I., Casas, D., Palomino, D., Vázquez, J.T., Estrada, F., Bárcenas, P., D'acremont, E., Gorini, C., 2019. 133,000 years of sedimentary record in a contourite drift in the western Alboran Sea: sediment sources and paleocurrent reconstruction. Geosciences 9 (8), 345. https://doi.org/10.3390/geosciences9080345.
MacAyeal, D.R., 1993. A low-order model of the Heinrich event cycle. Paleoceano 8, 767–773.
Macías, D., Garcia-Gorriz, E., Stips, A., 2016. The seasonal cycle of the Atlantic Jet dynamics in the Alboran Sea: direct atmospheric forcing versus Mediterranean thermohaline circulation. Ocean Dyn. 66 (2), 137–151.
Marshall, N.R., Piper, D.J.W., Saint-Ange, F., Campbell, D.C., 2014. Late Quaternary history of contourite drifts and variations in Labrador current flow, Flemish Pass, offshore eastern Canada. Geo-Mar. Lett. 34, 457–470.
Martín-Puertas, C., Jiménez-Espejo, F., Martínez-Ruiz, F., Nieto-Moreno, V., Rodrigo, M., Matas, M.P., Valero-Garcés, 2010. Late Holocene climate variability in the southwestern Mediterranean region: an integrated marine and terrestrial geochemical approach. Clim. Past 6, 807–816.
Martrat, B., Grimalt, J.O., López-Martínez, C., Cacho, I., Sierro, F.J., Flores, J.A., Zhang, R., Canals, M., Curtis, J.H., Hodell, D.A., 2004. Abrupt Temperature changes in the Western Mediterranean over the past 250,000 years. Science 306, 1762–1765. https://doi.org/10.1126/science.1101706.
Masqué, P., Fabres, J., Canals, M., Sánchez-Cabeza, J.A., Sánchez-Vidal, A., Cacho, I., Calafat, A., Bruach, J.M., 2003. Accumulation rates of major constituents of hemipelagic sediments in the deep Alboran Sea: a centennial perspective of sedimentary dynamics. Mar. Geol. 193 (3), 207–233.
Masson, D.G., Plets, R.M.K., Huvenne, V.A.I., Wynn, R.B., Bett, B.J., 2010. Sedimentology and depositional history of Holocene sandy contourites on the lower slope of the Faroe-Shetland Channel, Northwest of the UK. Mar. Geol. 268, 85–96.
Mayewski, P.A., Meeker, L.D., Twickler, M.S., Whitlow, S., Yang, Q., Lyons, W.B., Prentice, M., 1997. Major features and forcing of high-latitude northern hemisphere atmospheric circulation using a 110000-year-long glacio chemical series. J. Geophys. Res. 102 (C12), 26,345–26,366.
Mayewski, P.A., Rohling, E.J., Stager, J.C., Karlen, W., Maasch, K.A., Meeker, L.D., Meyerson, E.A., Gasse, F., van Kreveld, S., Holmgren, K., Lee-Thorp, J., Rosqvist, G., Rack, F., Staubwasser, M., Schneider, R.R., Steig, E., 2004. Holocene climate variability. Quat. Res. 62 (3) https://doi.org/10.1016/j.yqres.2004.07.001.
McCave, I.N., 2008. Size sorting during transport and deposition of fine sediments: Sortable silt and flow speed. In: Rebesco, M., Camerlenghi, A. (Eds.), Development in Sedimentology. Elselvier, pp. 121–142.
McCave, I.N., Manighetti, B., Robinson, S.G., 1995. Sortable silt and fine sediment size/composition slicing: parameters for palaeocurrent speed and palaeoceanography. Paleoceanog 10, 593–610.
McCave, I.N., Thornalley, D.J.R., Hall, J.R., 2017. Relation of sortable silt grain-size to deep-sea current speeds: calibration of the "Mud Current Meter". Deep-Sea Res. Part I: Oceanogr. Res. Papers 127, 1–12.
McCracken, K.G., Beer, J., Steinhilber, F., Abreu, J., 2013. A phenomenological study of the cosmic ray variations over the past 9400 years, and their implications regarding solar activity and the solar dynamo. Sol. Phys. 286, 609–627.
Millot, C., 2009. Another description of the Mediterranean Sea outflow. Progr. Ocean. 82, 101–124.
Miramontes, E., Cattaneo, A., Jouet, G., Théreau, E., Thomas, Y., Rovere, M., Cauquil, E., Trincardi, F., 2016. The Pianosa Contourite Depositional System (Northern Tyrrhenian Sea): drift morpho,logy and Plio-Quaternary stratigraphic evolution. Mar. Geol. 378, 20–42.
Moreno, E., Thouveny, N., Delanghe, D., McCave, I.N., Shackleton, N., 2002. Climatic and oceanographic changes in the Northeast Atlantic reflected by magnetic properties of sediments deposited on the Portuguese. Earth Planet. Sci. Lett. 202 (2), 465–480.
Moreno, A., Cacho, I., Canals, M., Grimalt, J.O., Sánchez-Vidal, A., 2004. Millennial-scale variability in the productivity signal from the Alboran Sea record, Western Mediterranean Sea. Palaeogeogr. Palaeoclimatol. Palaeoecol. 211 (3), 205–219.
Moreno, A., Cacho, I., Canals, M., Grimalt, J., Sánchez-Goñi, F., Schackleton, N., Sierro, F.J., 2005. Links between marine and atmospheric processes oscillating on a millennial timescale. A multi-proxy study of the last 50,000 yr from the Alboran (Western Mediterranean Sea). Quat. Sci. Rev. 24, 1623–1636.
Naranjo, C., García Lafuente, J., Sánchez Garrido, J.C., Sánchez Román, A., Delgado, Cabello J., 2012. The Western Alboran Gyre helps ventilate the Western Mediterranean Deep Water through Gibraltar. Deep Sea Res. Part I: Oceanogra. Res. Papers 63 (0), 157–163.
Nieto-Moreno, V., Martínez-Ruiz, F., Giralt, S., Jiménez-Espejo, F., Gallego-Torres, D., Rodrigo-Gámiz, M., García-Orellana, J., Ortega-Huertas, M., de Lange, G.J., 2011. Tracking climate variability in the western Mediterranean during the Late Holocene: a multiproxy approach. Clim. Past 7, 1395–1414.
Oppo, D.W., McManus, J.F., Cullen, J.L., 1998. Abrupt climate events 500,000 to 340,000 years ago: evidence from subpolar North Atlantic sediments. Science 279, 1335–1338.
Pardo-Igúzquiza, E., Rodríguez-Tovar, F.J., 2011. Implemented Lomb-Scargle Periodogram: a valuable tool for improving cyclostratigraphic research on unevenly sampled deep-sea stratigraphic sequences. Geo-Mar. Lett. 31 (5), 537–545.
Parrilla, G., Kinder, T.H., Preller, R., 1986. Deep and intermediate Mediterranean water in the western Alboran Sea. Oceanogr. Res. Paper 33 (1), 55–58. https://doi.org/10.1016/0198-0149(86)90108-1.
Peliz, A., Boutov, D., Teles-Machado, A., 2013. The Alboran Sea mesoscale in a long term high resolution simulation: statistical analysis. Ocean Model 72, 32–52.
Pérez-Asensio, J.N., Frigola, J., Pena, L.D., Sierro, F.J., Reguera, M.I., Rodríguez-Tovar, F.J., Dorador, J., Asioli, A., Kuhlmann, J., Huhn, K., Cacho, I., 2020. Changes in Western Mediterranean thermohaline circulation in association with a deglacial Organic Rich Layer formation in the Alboran Sea. Quat. Sci. Rev. 228 https://doi.org/10.1016/j.quascirev.2019.106075.
Pérez-Folgado, M., Sierro, F.J., Flores, J.A., Cacho, I., Grimalt, J.O., Zahn, R., Shackleton, N., 2003. Western Mediterranean planktonic foraminifera events and millennial climatic variability during the last 70 kyr. Mar. Micropaleontol. 48 (1–2), 49–70.
Petrovid, A., Lantzsch, H., Schwenk, T., Marquardt, J., Tischanack, J., Hanebuth, T.J.J., 2019. Post-LGM upward shift of the Mediterranean Outflow water recorded in a contourite drift off NW Spain. Mar. Geol. 407, 334–349.

Prins, M.A., Weltje, G.J., 1999. End-member modelling of siliciclastic grain-size distributions: The Late Quaternary record of eolian and fluvial sediment supply to the Arabian Sea and its paleoclimatic significance. In: Harbaugh, J., et al. (Eds.), Numerical Experiments in Stratigraphy: Recent Advances in Stratigraphic and Sedimentologic Computer Simulations. SEPM Special Publication 62, Soc. Sedimentary Geol, pp. 91–111.

Prins, M.A., Bouwer, L.M., Beets, C.J., Troelstra, S.R., Weltje, G.J., Kruk, R.W., Kuijpers, A., Vroon, P.Z., 2002. Ocean circulation and iceberg discharge in the glacial North Atlantic: inferences from unmixing of sediment size distributions. Geology 30, 555–558.

Rahmstorf, S., 2006. Thermohaline Ocean Circulation. Encyclopedia of Quaternary Sciences, Amsterdam.

Rebesco, M., Carmelenghi, A., 2008. Contourites, Developments in Sedimentology 60, first ed. Elsevier, Amsterdam.

Rebesco, M., Wahlin, A., Laberg, J.S., Schauer, U., Beszczynska-Möller, Y., Diviacco, P., 2013. Quaternary contourite drifts of the Western Spitsbergen margin. Deep-Sea Res. I 179, 156–168.

Rebesco, M., Hernández-Molina, F.J., Van Rooij, D., Wåhlin, A., 2014. Contourites and associated sediments controlled by deep-water circulation processes: State-of-the-art and future considerations. Mar. Geol. 352, 111–154.

Rebesco, A., Ozmaral, A., Urgeles, R., Accettella, D., Lucchi, R.L., Rüther, D., Winsborrow, M., Llopart, J., Caburlotto, A., Lantzsch, H., Hanebuth, T.B., 2016. Evolution of a high-latitude sediment drift inside a glacially-carved trough based on high-resolution seismic stratigraphy (Kveithola, NW Barents Sea). Quat. Sci. Rev. 146, 178–193.

Reimer, P.J., Bard, E., Bayliss, A., Beck, J.W., Blackwell, P.G., Ramsey, C.B., Buck, C.E., Cheng, H., Edwards, R.L., Friedrich, M., Grootes, P.M., Guilderson, P.M., Haflidason, H., Hajdas, I., Hatté, C., Heaton, T.J., Hoffmann, D.L., Hoff, A.G., Hughen, K.A., Kaiser, K.F., Kromer, B., Manning, S.W., Niu, M., Reimer, R.W., Richards, D.A., Scott, E.M., Southon, J.R., Staff, R.A, Turney, C.S.M., vander Plicht, J., 2013. IntCal13 and Marine13 Radiocarbon Age Calibration Curves 0–50,000 years cal BP. Radiocarbon 55 (4), 1869–1887. https://doi.org/10.2458/azu_js_rc.55.16947.

Revel, M., Cremer, M., Grousset, F.E., Labeyrie, L., 1996. Grain-size and Sr-Nd as tracer of paleo-bottom current strength, Northeast Atlantic Ocean. Mar. Geol. 131, 233–249.

Roberts, J., McCave, I.N., McChynont, E.L., Kender, S., Hillenbrand, C.D., Matano, R., Hodel, D.A., Peck, V.L., 2017. Deglacial changes in flow and frontal structure through the Dake Passage. Earth Planet. Sc. Lett. 474, 397–408.

Rodrigo-Gámiz, M., Martínez-Ruiz, F., Jiménez-Espejo, F.J., Gállego-Torres, D., Nieto-Moreno, V., Romero, O., Ariztegui, D., 2011. Impact of climate variability in the western Mediterranean during the last 20,000 years: oceanic and atmospheric responses. Quat. Sci. Rev. 30, 2018–2034.

Rodrigo-Gámiz, M., Martínez-Ruiz, F., Rodríquez-Tovar, F.J., Jiménez-Espejo, F.J., Pardo-Igúzquiza, E., 2014. Millennial to centennial scale climate periodicity and forcing mechanisms in the western Mediterranean for the past 20000 yr. Quat. Res. 81, 78–93.

Rodrigo-Gámiz, M., Martínez-Ruiz, F., Rodríguez-Tovar, F.J., Pardo-Igúzquiza, E., Ortega-Huertas, M., 2018. Appraising timing response of paleoenvironmental proxies to the Bond cycle in the western Mediterranean over the last 20 kyr. Clim. Dyn. 50, 2925–2934. https://doi.org/10.1007/s00382-017-3782-y.

Rodríguez-Tovar, F.J., Dorador, J., 2015. Ichnofabric characterization in cores: a method of digital image treatment. Annal. Societ. Geol. Pol. 85, 465–471.

Rodríguez-Tovar, F.J., Reolid, M., Pardo-Igúzquiza, E., 2010. Planktonic versus benthic foraminifera response to Milankovitch forcing (Late Jurassic, Betic Cordillera): Testing methods for cyclostratigraphic analysis. Facies 56, 459–470.

Rodríguez-Tovar, F.J., Miguez-Salas, O., Hernández-Molina, F.J., Hüneke, H., 2019c. First record of graphoglyptids in Cyprus: Indicative presence of turbidite deposits at the Pakhna Formation. First record of graphoglyptids in Cyprus: indicative presence of turbidite deposits at the Pakhna Formation. Ichnos 27 (2), 237–243. https://doi.org/10.1080/10420940.2019.1688801.

Rodríguez-Tovar, F.J., Hernández-Molina, F.J., Hüneke, H., Llave, E., Stow, D., 2019a. Contourite facies model: improving contourite characterization based on the ichnological analysis. Sediment. Geol. 384, 60–69.

Rodríguez-Tovar, F.J., Hernández-Molina, F.J., Hüneke, H., Chiarella, D., Llave, E., Mena, A., Miguez-Salas, O., Dorador, J., De Castro, S., Stow, D.A.V., 2019b. Key evidence for distal turbiditic-and bottom-current interactions from tubular turbidite infills. Palaeogeogr. Palaeoclimatol. Palaeoecol. 533, 109233.

Rogerson, M., Rohling, E.J., Weaver, P.P.E., Murray, W., 2005. Glacial to interglacial changes in the settling depth of the Mediterranean outflow plume. Paleoceanogr 20, PA3007. https://doi.org/10.1029/2004PA001106.

Rogerson, M., Cacho, I., Jiménez-Espejo, J., Reguera, M.I., Sierro, F.J., Martínez-Ruiz, F., Frigola, J., Canals, M., 2008. A dynamic explanation for the origin of the western Mediterranean organic-rich layers. Geochem. Geophys. Geosyst. 9 https://doi.org/10.1029/2007GC001936.

Rogerson, M., Bigg, G.R., Rohling, E.J., Ramirez, J., 2012. Vertical density gradient in the eastern North Atlantic during the last 30000 years. Clim. Dyn. 39, 589–598.

Rojo-Garibaldi, R., Salas-de-León, D., Monreal-Gómez, M.A., Giannerini, S., Castwright, J.H.E., 2020. Chaos and periodicities in a climatic time series of the Iberian Margin. Chaos 30, 063126. https://doi.org/10.1063/1.5123509.

Sánchez-Leal, R.F., Bellanco, M.J., Fernández-Salas, L.M., García-Lafuente, J., Gasser-Rubinat, M., González-Pola, C., Hernández-Molina, F.J., Pelegrí, J.L., Peliz, A., Relvas, P., Roque, D., Ruiz-Villarreal, M., Sammartino, S., Sánchez-Garrido, J.C., 2017. The Mediterranean Overflow in the Gulf of Cadiz: a rugged journey. Sci. Adv. 3 (11) https://doi.org/10.1126/sciadv.aao0609 art. no. eaao0609.

Sanchez-Vidal, A., Calafat, A., Canals, M., Frigola, J., Fabres, J., 2005. Particle fluxes and organic carbon balance across the Eastern Alboran Sea (SW Mediterranean Sea). Cont. Shelf Res. 25, 609–628. https://doi.org/10.1016/j.csr.2004.11.004.

Scargle, J.D., 1982. Studies in astronomical time series analysis. II. Statistical aspects of spectral analysis of unevenly spaced data. Astrophys. J. 263, 835–853.

Shor, A.N., Kent, D.V., Flood, R.D., 1984. Contourite or turbidite?: Magnetic fabric of fine-grained Quaternary sediments, Nova Scotia continental rise. In: Stow, D.A.V., Piper, D.J.W. (Eds.), Fine Grained sediments: Deep Water Processes and Facies. Geological Society, London, Special Publications 15, London, pp. 257–273.

Sierro, F.J., Hodel, D.A., Curti, J.H., Flores, J.A., Reguer, I., Colmenero-Hidalgo, E., Barcena, M.A., Grimalt, J.O., Cacho, I., Frigola, F., Canals, M., 2005. Impact of iceberg melting in the Mediterranean thermohaline circulation during Heinrich events. Paleooceanogr 20, PA2019.

Smillie, Z., Stow, D., Esentia, I., 2018. Deep-sea contourite drifts, erosional features and bedforms. In: Cochran, J.K. (Ed.), Encyclopedia of Ocean Sciences, 4. Elsevier, pp. 97–110.

Speich, S., Madec, G., Crépon, M., 1995. A Strait Outflow circulation process study: the Case of the Alboran Sea. J. Phys. Oceanogr. 26, 320–340.

Spooner, P., Thornalley, D.J.R., Ellis, P., 2018. Grain size constraints on glacial circulation in the Southwest Atlantic. Paleoocean. Paleoclimatol. 33, 21–30.

Stanley, D.J., Kelling, G., Vera, J.A., Sheng, H., 1975. Sands in the Alboran Sea: a model of input in a Deep Marine Basin. Smith. Contri. to the Earth Sci. 1–51. https://doi.org/10.5479/si.00810274.15.1.

Stoker, M.S., Akhurst, M.C., Howe, J.A., Stow, D.A.V., 1998. Sediment drifts and contourites on the continental margin off Northwest Britain. Sediment. Geol. 115 (1–4), 33–51.

Stommel, H., Byrden, H., Malgelsdorf, P., 1973. Does the Mediterranean outflow come from great depth? Pure Appl. Geophys. 105, 879–889.

Stow, D.A.V., Faugères, J.C., 2008. Contourites facies and the facies model. In: Rebesco, M., Camerlengui, A. (Eds.), Contourites, Developments In Sedimentology, Amsterdam, pp. 223–256.

Stow, D., Lowell, J.P.B., 1979. Contourites: their recognition in modern and ancient sediments. Earth Sci. Rev. 14 (3), 251–291.

Stow, D.A.V., Piper, D.J.W., 1984. Deep-water fine-grained sediments: Facies models. In: Stow, D.A.V., Piper, D.J.W. (Eds.), Fine-Grained sediments: Deep-Water Processes and Facies. Geological Society of London, Special Publications 15, London, pp. 611–646.

Stow, D., Smillie, Z., 2020. Distinguishing between deep-water sediment facies: turbidites, contourites and hemipelagites. Geosciences 10 (68). https://doi.org/10.3390/geosciences10020068.

Stow, D.A.V., Alam, M., Piper, D.J.W., 1984. Sedimentology of the Halifax Formation, Nova Scotia: Lower Palaeozoic fine-grained turbidites. In: Stow, D.A.V., Piper, D.J.W. (Eds.), Fine-Grained sediments: Deep-Water Processes and Facies. Geological Society of London, Special Publications 15, London, pp. 127–144.

Stow, D., Faugères, J.C., Howe, J.A., Pudsey, C.J., Viana, A.R., 2002. Bottom currents, contourites and deep-sea sediment drifts: Current state-of-the-art. In: Stow, D.A.V., Pudsey, C.J., Howe, J.A., Faugères, J.C., Viana, A.R. (Eds.), Deep-Water Contourite Systems: Modern Drifts and Ancient Series, Seismic and Sedimentary Characteristics Geological Society. London Memoirs 22(1), London, pp. 7–20.

Stow, Smillie, Z., Pan, J., Esentia, I., 2018. Deep-Sea Contourites: Sediments and Cycles. Encyclopedia of Ocean Sciences: Earth Systems and Environmental Sciences, third ed. Elsevier. https://doi.org/10.1016/B978-0-12-409548-9.10879-6.

Stuiver, M., Reimer, P.J., 1993. Extended 14C data base and revised CALIB 3.0 '4C age calibration program. Radiocarbon 35 (1), 215–230.

Toucanne, S., Mulder, T., Schönfeld, J., Hanquiez, V., Gonthier, E., Duprat, J., Cremer, M., Zaragosi, S., 2007. Contourites of the Gulf of Cadiz: a high-resolution record of the paleocirculation of the Mediterranean Outflow Water during the last 50000 years. Mar. Geol. 246 (2–4), 354–366.

Udden, J.A., 1914. Mechanical composition of clastic sediments. Geol. Soc. Am. Bull. 25, 655–744.

Vandorpe, T., Collart, T., Cnude, V., Lebreiro, S., Hernández-Molina, J.J., Alonso, B., Mena, A., Antón, L., Van Rooij, D., 2019. Quantitative characterization of contourite deposits using medical CT. Mar. Geol. 417 https://doi.org/10.1016/j.margeo.2019.106003.

Vargas-Yáñez, Plaza, F., García-Lafuente, J., Sarhan, T., Varga, J.M., Vélez-Belchi, P., 2002. About the seasonal variability of the Alboran Sea circulation. J. Mar. Syst. 35, 229–248.

Verdicchio, G., Trincardi, F., 2008. Mediterranean shelf-edge muddy contourites: examples from the Gela and South Adriatic basins. Geo-Mar. Lett. 28, 137–151.

Weltje, G.J., 1997. End-member modeling of compositional data: numerical-statistical algorithms for solving the explicit mixing problem. Math. Geol. 29, 503–549.

Wentworth, C.K., 1922. A scale of grade and class terms for clastic sediments. J. Geol. 30, 377–392.

Wetzel, A., 1984. Bioturbation in deep-sea fine-grained sediments: Influence of sediment texture, turbidite frequency and rates of environmental change. In: Stow, D.A.V., Piper, D.J.W. (Eds.), Fine-Grained Sediments: Deep-Water Processes and Facies. Geological Society London, Special Publication 15, London, pp. 595–608.